

# Systematic classification of one-loop models addressing the $b \rightarrow s\nu\bar{\nu}$ anomaly

Xin-Shuai Yan,<sup>1,\*</sup> Wen-Feng Liu,<sup>1,†</sup> Qin Chang,<sup>1,‡</sup> and Ya-Dong Yang<sup>1,2,§</sup>

<sup>1</sup>*Institute of Particle and Nuclear Physics, Henan Normal University, Xinxiang, Henan 453007, China*

<sup>2</sup>*Institute of Particle Physics and Key Laboratory of Quark and Lepton Physics (MOE), Central China Normal University, Wuhan, Hubei 430079, China*

The recent evidence for the decay  $B^+ \rightarrow K^+\nu\bar{\nu}$  reported by the Belle II collaboration, combined with the existing constraints on the neutral mode  $B^0 \rightarrow K^{*0}\nu\bar{\nu}$ , implies a deviation from the Standard Model prediction that necessitates New Physics contributions to both left- and right-handed vector currents. We perform a systematic topological classification of renormalizable one-loop completions capable of generating the required dimension-six operators while forbidding tree-level mediation. Based on this classification, we identify and construct two minimal benchmark scenarios—a scalar-rich model and a fermion-rich model—and perform a comprehensive phenomenological analysis. Our study demonstrates that while these one-loop models can yield enhancements in the  $b \rightarrow s\nu\bar{\nu}$  branching fractions, the attainable magnitudes are significantly restricted by the combined effects of loop suppression and complementary flavor constraints, limiting their ability to fully accommodate the current anomaly.

## I. INTRODUCTION

Direct searches for new particles at the LHC have so far yielded null results, placing stringent constraints on physics beyond the Standard Model (SM). In contrast, indirect probes in the flavor sector exhibit persistent tensions. The flavor-changing neutral current (FCNC) transition  $b \rightarrow s\nu\bar{\nu}$  has recently emerged as a key area of interest. The Belle II collaboration reported the first evidence for  $B^+ \rightarrow K^+\nu\bar{\nu}$  with a branching fraction of  $\mathcal{B}_{\text{exp}} = (2.3 \pm 0.7) \times 10^{-5}$  [1], exceeding the SM prediction of  $(4.44 \pm 0.30) \times 10^{-6}$  [2] by  $2.7\sigma$ . This quark-level transition also governs the neutral mode  $B^0 \rightarrow K^{*0}\nu\bar{\nu}$ , where the current experimental upper limit of  $1.8 \times 10^{-5}$  [3] lies roughly a factor of two above the SM expectation of  $(9.47 \pm 1.40) \times 10^{-6}$  [2].

These findings have stimulated a wide range of theoretical interpretations. One class of models postulates the existence of light, invisible states—such as sterile neutrinos [4–13], light dark matter (DM) [14–22], axion-like particles [23–30], or generic long-lived particles [31–37]—which mimic the missing energy signature of the neutrino pairs. Alternatively, the anomalies can be addressed within the framework of heavy new physics (NP), where virtual exchanges of heavy mediators modify the Wilson coefficients of the low-energy effective Lagrangian [12, 18, 38–54]. Related phenomenological implications have also been discussed in Ref. [55].

These tensions can be further quantified by the ratio  $R \equiv \mathcal{B}(B^0 \rightarrow K^{*0}\nu\bar{\nu})/\mathcal{B}(B^+ \rightarrow K^+\nu\bar{\nu})$ , where the observed value  $R_{\text{exp}} = 0.38 \pm 0.31$  is significantly suppressed relative to the SM expectation of  $R_{\text{SM}} = 2.14 \pm 0.35$ . In the framework of low-energy effective theory (LEFT), assuming the neutrinos remain purely left-handed, scalar and tensor contributions vanish due to chirality constraints. Consequently, the relevant interactions are governed by the vector operators:

$$\begin{aligned} \mathcal{O}_V^L &= (\bar{s}\gamma_\mu P_L b)(\bar{\nu}_\ell\gamma^\mu P_L \nu_\ell), \\ \mathcal{O}_V^R &= (\bar{s}\gamma_\mu P_R b)(\bar{\nu}_\ell\gamma^\mu P_L \nu_\ell). \end{aligned} \quad (1)$$

Clearly, the discrepancy in  $R$  cannot be resolved by modifying only the left-handed operator  $\mathcal{O}_V^L$ , as this would simply rescale both rates while leaving the ratio invariant. Therefore, the introduction of the right-handed operator  $\mathcal{O}_V^R$  is necessary [42].

In contrast to previous studies within the heavy NP framework—which have typically focused either on a specific model or solely on the effective field theory—in this work we systematically investigate the ultraviolet origin of these effective interactions. We focus on completions that generate the required operators ( $\mathcal{O}_V^L$  and  $\mathcal{O}_V^R$ ) at the one-loop level via heavy new scalars and fermions. Radiative generation is a highly motivated strategy in particle physics; it offers a particularly economical pathway to reconcile multiple phenomena within a unified framework—akin to the simultaneous explanation of neutrino masses and dark matter in scotogenic scenarios (see e.g., Refs. [56–58]). Adopting this philosophy for the  $b \rightarrow s\nu\bar{\nu}$  sector, and guided exclusively by the SM gauge symmetry, we employ a diagrammatic method to generate the complete set of one-loop topologies

\* [yanxinshuai@htu.edu.cn](mailto:yanxinshuai@htu.edu.cn)

† [liuwenfeng2022@stu.htu.edu.cn](mailto:liuwenfeng2022@stu.htu.edu.cn)

‡ [changqin@htu.edu.cn](mailto:changqin@htu.edu.cn)

§ [yangyd@mail.ccnu.edu.cn](mailto:yangyd@mail.ccnu.edu.cn)

<sup>1</sup> Following the approach in Ref. [42], we interpret the experimental upper limit  $\mathcal{B}(B^0 \rightarrow K^{*0}\nu\bar{\nu}) < 1.8 \times 10^{-5}$  using a half-normal distribution. This yields a derived branching fraction of  $\mathcal{B}(B^0 \rightarrow K^{*0}\nu\bar{\nu}) = (0.87 \pm 0.66) \times 10^{-5}$ .

involving NP particles. We classify the minimal extensions capable of simultaneously generating both the left- and right-handed LEFT operators. However, given the substantial deviation of the experimental value from the SM prediction, combined with the loop suppression factor and stringent LHC mass constraints, a full resolution of the anomalies is expected to be non-trivial. We therefore quantitatively investigate the extent to which these loop effects can account for the observed tensions, while simultaneously satisfying the constraints from complementary flavor observables.

The remainder of this paper is organized as follows. In Sec. II, we present the systematic classification of one-loop topologies and identify the UV extensions capable of generating the required effective operators. Section III introduces two minimal benchmark models derived from this classification for detailed study. In Sec. IV, we define the relevant observables and establish the constraints on the Wilson coefficients imposed by experimental data. The phenomenological analysis of these models is presented in Sec. V. Finally, we summarize our findings in Sec. VI, with technical details provided in the Appendices.

## II. SYSTEMATIC CLASSIFICATION: FROM TOPOLOGIES TO MODELS

We begin our analysis by systematically classifying the possible one-loop realization of the dimension-six operators  $\mathcal{O}_V^L$  and  $\mathcal{O}_V^R$  defined in Eq. (1). A central requirement of our framework is that the one-loop contribution is the leading one, and therefore any tree-level realization of these effective operators shall be absent. This condition can be naturally enforced in various models through the imposition of a discrete or flavor symmetry in a manner analogous to established models of radiative neutrino mass generation (see e.g., Refs. [58–60]). As the introduction of such symmetries is a standard technique in model-building, we proceed with the assumption that a suitable symmetry can always be implemented to forbid the tree-level contributions. Consequently, we will not specify the exact symmetry structure for each case but will instead focus on the general classification of all valid one-loop model structures.

Our classification scheme is built upon a hierarchy of concepts [60], which we define as follows:

- **Topology:** We define a *topology* as the underlying graphical structure of a Feynman diagram, abstracting from the physical properties of the particles involved. It is defined solely by its vertices and their connectivity, without consideration for the Lorentz nature or quantum numbers of the fields.
- **Renormalizable Topology:** A topology is deemed *renormalizable* if it can be constructed exclusively from vertices corresponding to interactions of mass dimension less than or equal to four. This ensures that the corresponding operator can be embedded within a renormalizable quantum field theory.
- **Diagram:** We refer to a topology as a *diagram* once a specific particle type (i.e., scalar, vector, or fermion) has been assigned to each line.
- **Model-Diagram:** A *model-diagram* is a fully specified diagram where all internal fields are assigned a complete set of quantum numbers under relevant symmetries (e.g., SM gauge group representations).

We begin our classification by systematically generating all one-loop topologies for a four-point interaction using only three- and four-point vertices. From this initial set, we discard all graphs corresponding to tadpoles or external-line self-energy corrections, as they lead to divergent loop integrals. This leaves six topologies, which we depict in Fig. 1.

We categorize these six topologies according to the definitions established previously. The first class, comprising T1 and T2, is composed exclusively of three-point vertices and is therefore classified as *renormalizable*. In contrast, the remaining topologies—T3, T4, T5, and T6—each contain at least one four-point vertex. Given that all external lines in our operators are fermionic, any such four-point vertex necessarily corresponds to an operator with a mass dimension greater than four. Consequently, these latter four topologies are classified as *non-renormalizable* and will not be considered further in this work.

We now proceed to construct the diagrams for the renormalizable topologies T1 and T2. By assigning fermion and scalar identities to the internal lines while keeping the four external lines as fermions, we obtain the three distinct diagrams shown in Fig. 2. In our convention, solid lines denote fermions and dashed lines denote scalars. These diagrams are distinguished by their structure, which we categorize as either reducible or irreducible. Here we deem a one-loop diagram *reducible* if it functions as a radiative correction to a renormalizable vertex. Accordingly, diagram T1-1 is an irreducible box diagram, while T2-1 and T2-2 are reducible, each containing a one-loop vertex correction as highlighted in red.

This structural distinction has a critical physical implication. The presence of a reducible vertex correction, as seen in T2-1 and T2-2, generically implies the existence of a corresponding tree-level diagram that contributes to the same four-point operator. To ensure the one-loop contribution is dominant without fine-tuning or the imposition of special symmetries to forbid the tree-level term, such diagrams must be set aside. Furthermore, the loop integral in diagram T2-2 (enclosed in the green-dashed box) is UV divergent. For these reasons, we will focus our subsequent analysis on the irreducible T1-1 diagram, which represents a *genuine*

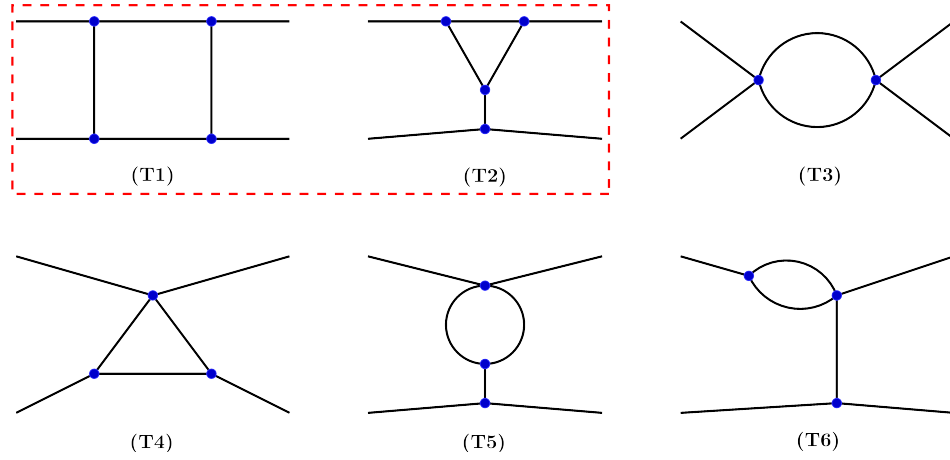


Figure 1. One-loop topologies with 3- and 4-point vertices and four external legs. Topologies T1 and T2, highlighted in the red-dashed box, are renormalizable.

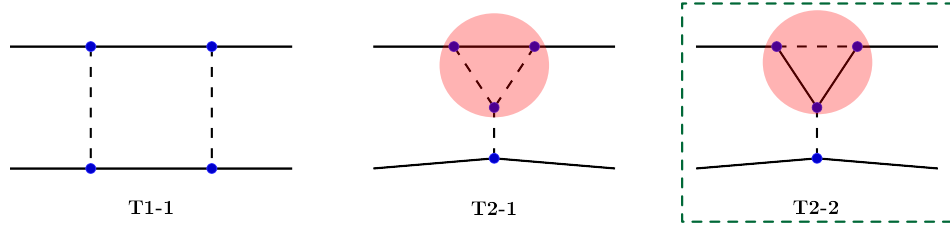


Figure 2. Possible one-loop diagrams for the topologies T1 and T2, where the dashed lines denote scalars and the solid lines denote fermions. All the diagrams for T2 contain a reducible 3-point loop vertex, highlighted in red. The diagram T2-2, enclosed in the green-dashed box, possesses an ultraviolet divergent loop integral.

one-loop realization [59, 60]. We comment, however, that the diagram T2-1 remains a perfectly viable candidate in models once a symmetry is explicitly imposed to forbid its tree-level counterpart.

Table I. SM gauge quantum number assignments for the internal fields of diagram (c) that generate the operator  $\mathcal{O}_V^L$ . The  $SU(3)_c$  and  $SU(2)_L$  representations are presented as distinct cases, while the  $U(1)_Y$  hypercharges are fixed relative to a single free parameter,  $\alpha = Y_{\Psi_1}$ .

$SU(3)_c$	$\Psi_1$	$X_2$	$\Psi_3$	$X_4$
A	1	$\bar{3}$	$\bar{3}$	$\bar{3}$
B	3	1	1	1
$SU(2)_L$	$\Psi_1$	$X_2$	$\Psi_3$	$X_4$
I	1	2	3	2
II	2	1	2	1
II	2	1	2	3
IV	3	2	1	2
V	3	2	3	2
VI	2	3	2	1
VII	2	3	2	3
$U(1)_Y$	$\Psi_1$	$X_2$	$\Psi_3$	$X_4$
i	$\alpha$	$\alpha - 1/6$	$\alpha - 2/3$	$\alpha - 1/6$

With the T1-1 diagram established as our template, the next step is to construct its concrete physical realizations. We assign a specific particle content to the internal lines: two vector-like fermions ( $\Psi_1, \Psi_3$ ) and two scalars ( $X_2, X_4$ ). We then attach

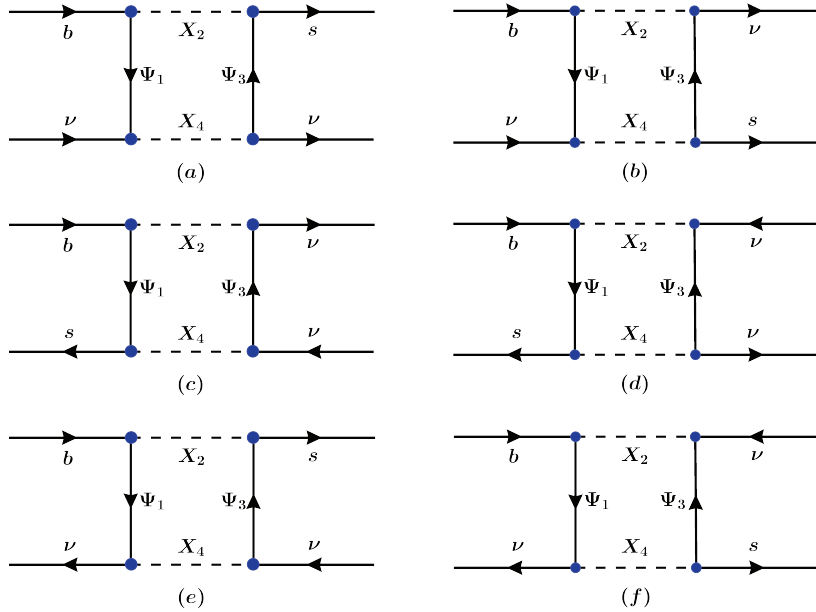


Figure 3. The six distinct diagrams that can be constructed from the T1-1 diagram by permuting the external fields ( $b, s, \nu, \bar{\nu}$ ). The internal fields are fixed as fermions ( $\Psi_1, \Psi_3$ ) and scalars ( $X_2, X_4$ ).

the external fields—a  $b$  quark, an  $s$  quark, and two neutrinos ( $\nu$ )—in all non-equivalent configurations, leaving their chirality unspecified at this stage. This procedure yields the six unique diagrams depicted in Fig. 3. For notational simplicity, we drop the “T1-1” prefix and will henceforth refer to these diagrams by their labels, (a) through (f).

We now promote the diagrams to *model-diagrams* by assigning SM quantum numbers to the internal fields, requiring SM gauge symmetry conservation at each vertex. The quantum numbers of the external fields provide the necessary boundary conditions, fixed by the choice of target operator ( $\mathcal{O}_V^R$  or  $\mathcal{O}_V^L$ ). For operators involving  $SU(2)_L$  charges, we note that the external left-handed fermions shall be treated as components of their respective doublets: the  $b$  and  $s$  quarks as part of the quark doublet  $Q$ , and the neutrino as part of the lepton doublet  $L$ . The nature of the constraints on the internal fields then depends on the gauge group. For  $U(1)_Y$ , the additive nature of hypercharge means that a choice for one internal field’s hypercharge fixes all others. For  $SU(3)_c$  and  $SU(2)_L$ , however, the tensor product of representations decomposes into multiple irreducible representations, allowing for more freedom. In this work, to ensure a tractable classification, we restrict our analysis to color singlet and triplet for  $SU(3)_c$ , and  $SU(2)_L$  representations up to triplet.

As a representative example, we detail in Table I the complete set of allowed SM quantum number assignments for the internal fields of diagram (c) that generate the operator  $\mathcal{O}_V^L$ . The analogous results for the remaining five diagrams are compiled in Appendix C. The table is organized into three sections, listing the viable assignments for the  $SU(3)_c$  and  $SU(2)_L$  representations, and the corresponding  $U(1)_Y$  hypercharges. Each physical model is constructed by selecting one complete set of  $SU(3)_c$  representations (e.g., case A) and one set of  $SU(2)_L$  representations (e.g., case I). The hypercharges are not independent; as shown in the final section, they are all uniquely determined by the choice of a single free parameter,  $\alpha$ , which we define as the hypercharge of the fermion  $\Psi_1$  ( $\alpha \equiv Y_{\Psi_1}$ ).

A crucial aspect of this analysis is the matching procedure between the high-scale UV model and the low-energy effective operators. When integrating out the heavy internal fields, the UV model does not directly generate the LEFT operators  $\mathcal{O}_V^{L,R}$ . Instead, at the new physics scale  $\Lambda$ , it must first be matched onto the appropriate set of dimension-six operators in the Standard Model Effective Field Theory (SMEFT). For the processes we consider, the relevant SMEFT Lagrangian is

$$\mathcal{L}_{\text{SMEFT}} \supset [C_{\ell d}]_{prst} Q_{\ell d} + [C_{\ell q}^{(1)}]_{prst} Q_{\ell q}^{(1)} + [C_{\ell q}^{(3)}]_{prst} Q_{\ell q}^{(3)}, \quad (2)$$

where the operators are defined as

$$\begin{aligned} Q_{\ell d} &= (\bar{L}_p \gamma^\mu L_r)(\bar{d}_{Rs} \gamma_\mu d_{Rt}), \\ Q_{\ell q}^{(1)} &= (\bar{L}_p \gamma^\mu L_r)(\bar{Q}_s \gamma_\mu Q_t), \\ Q_{\ell q}^{(3)} &= (\bar{L}_p \gamma^\mu \tau^I L_r)(\bar{Q}_s \gamma_\mu \tau^I Q_t), \end{aligned} \quad (3)$$

with  $\tau^I$  being the Pauli matrices and  $p, r, s, t$  the generation indices. In our calculation, we adopt two primary conventions. First, the new physics scale  $\Lambda$  is absorbed into the definition of the Wilson coefficients. Second, we work in the “down basis,” where the down-type quark and charged-lepton Yukawa matrices are diagonal. Within this framework, the SMEFT operators must then be evolved via renormalization group (RG) running from the high scale down to the electroweak scale, where they can be matched onto the LEFT operator basis, which includes  $\mathcal{O}_V^L$  and  $\mathcal{O}_V^R$  [61].

To illustrate this procedure, we perform an explicit calculation for a representative case: model A-V, constructed from diagram (c) using the  $SU(3)_c$  and  $SU(2)_L$  assignments from cases A and V in Table I, respectively. For simplicity, we assume that the scalars  $X_2$  and  $X_4$  are the same particle, as they share the same SM quantum numbers. The interaction Lagrangian for this model is given by

$$\begin{aligned} \mathcal{L} &\supset g_1^t \bar{\Psi}_1 Q_t X_2 + g_2^p \bar{L}_p \Psi_3 X_2^\dagger + g_2^{r*} \bar{\Psi}_3 L_r X_2 + g_1^{s*} \bar{Q}_s \Psi_1 X_2^\dagger \\ &= g_1^t \bar{\Psi}_1^A Q_{t\alpha} X_{2\alpha'} \xi_{\alpha\alpha'}^A + g_2^p \bar{L}_{p\beta} \Psi_3^B X_{2\beta'}^* (\xi^{B\dagger})_{\beta\beta'} + g_2^{r*} \bar{\Psi}_3^{A'} L_{r\rho} X_{2\rho'} \xi_{\rho\rho'}^{A'} + g_1^{s*} \bar{Q}_{s\sigma} \Psi_1^{B'} X_{2\sigma'}^* (\xi^{B'\dagger})_{\sigma\sigma'}, \end{aligned} \quad (4)$$

where in the second line we have made the  $SU(2)_L$  structure explicit. The Greek letters  $(\alpha, \beta, \dots)$  are used to denote  $SU(2)_L$  indices in the fundamental representation, taking values 1 and 2, while color indices are suppressed due to the trivial  $SU(3)_c$  structure of this model. The letters  $g_{1,2}$  denote the coupling constants, and the  $SU(2)_L$  tensor  $\xi$  is defined as  $\xi^A = ((1 + \tau^3)/2, \tau^1/\sqrt{2}, (1 - \tau^3)/2)$  with  $A \in 1, 2, 3$ .

Integrating out the heavy fields  $\Psi_i$  and  $X_2$  at one loop yields the following effective four-fermion operator:

$$\mathcal{L}_{\text{eff}} \supset (g_1^t g_2^p g_2^{r*} g_1^{s*}) J_4(m_{X_2}, m_{X_2}, m_{\Psi_1}, m_{\Psi_3}) \left( \bar{L}_{p\beta} \gamma^\mu L_{r\rho} \right) \left( \bar{Q}_{s\sigma} \gamma_\mu Q_{t\alpha} \right) \xi_{\alpha\alpha'}^A (\xi^{B\dagger})_{\beta\alpha'} (\xi^{A\dagger})_{\sigma\rho'} \xi_{\rho\rho'}^B, \quad (5)$$

where  $J_4$  is the loop function defined in Appendix A. The final step is to evaluate the product of the  $SU(2)_L$  tensors in Eq. (5). This algebraic simplification directly maps the operator onto a specific linear combination of the SMEFT operators  $Q_{\ell q}^{(1)}$  and  $Q_{\ell q}^{(3)}$ . The final effective Lagrangian at the scale  $\Lambda$  is therefore

$$\mathcal{L}_{\text{eff}} = \frac{1}{8} (g_1^t g_2^p g_2^{r*} g_1^{s*}) J_4(m_{X_2}, m_{X_2}, m_{\Psi_1}, m_{\Psi_3}) \left( 9 [Q_{\ell q}^{(1)}]_{prst} + [Q_{\ell q}^{(3)}]_{prst} \right). \quad (6)$$

The Wilson coefficients for the SMEFT operators are thus determined by the couplings and masses of the UV model. For the convenience of future reference, we list the coefficients of  $Q_{\ell q}^{(1)}$  and  $Q_{\ell q}^{(3)}$  for all valid models in Table II.

We highlight two important features of this classification. First, not all gauge-invariant solutions are phenomenologically viable. There exist certain  $SU(2)_L$  assignments—such as the case where  $(\Psi_1, X_2, \Psi_3, X_4)$  transform as  $(1, 2, 1, 2)$ —which generate an  $SU(2)_L$  structure of the form

$$\left( \bar{L}_{p\alpha} \gamma^\mu L_{r\beta} \right) \left( \bar{Q}_{s\beta} \gamma_\mu Q_{t\alpha} \right) = \frac{1}{2} \left( [Q_{\ell q}^{(1)}]_{prst} + [Q_{\ell q}^{(3)}]_{prst} \right). \quad (7)$$

After electroweak symmetry breaking, the tree-level matching of this specific combination of SMEFT operators onto the target LEFT operator  $\mathcal{O}_V^L$  yields a vanishing Wilson coefficient. For this reason, solutions leading to this null result have been excluded from our final analysis, presented in Table II and throughout Appendix C.

Second, our analysis reveals a correspondence between a diagram’s structure and the operator chirality it can generate, under the assumption that the mediating fields are complex (i.e., Dirac fermions and complex scalars). In this scenario, diagrams (c) and (d) are versatile, capable of generating both  $\mathcal{O}_V^L$  and  $\mathcal{O}_V^R$ . In contrast, the other diagrams exclusively generate a single chirality: diagrams (a) and (b) are restricted to  $\mathcal{O}_V^R$ , while (e) and (f) are restricted to  $\mathcal{O}_V^L$ . However, this clear distinction is lifted if the model contains real fields (Majorana fermions or real scalars). In such cases, new interaction structures become possible, allowing diagrams that were previously restricted to a single chirality to generate both. This will be explicitly illustrated by our benchmark models in Sec. III.

Finally, we consider the possibility that one of the new internal fields could serve as a DM candidate. Any viable candidate must be stable on cosmological timescales and must be a color-singlet and electrically neutral. The most stringent constraints on such models often arise from DM direct detection experiments, such as PandaX-4T [62] and XENONnT [63]. To ensure these bounds are satisfied, we impose the condition that the DM candidate has zero hypercharge,  $Y = 0$ , as the direct detection cross section is typically proportional to the hypercharge squared. Since the electric charge is given by  $Q_{\text{em}} = T_3 + Y$ , the requirements of electrical neutrality and zero hypercharge together imply that the candidate must also have  $T_3 = 0$ . This condition generally disfavors  $SU(2)_L$  multiplets with an even number of components (e.g., doublets). A well-known exception is the scalar doublet, where a mass splitting between its components can suppress the tree-level Z-boson coupling, allowing it to evade direct detection bounds [64, 65].

Table II. Relative strengths of the SMEFT operators  $Q_{\ell q}^{(1)}$  and  $Q_{\ell q}^{(3)}$  generated by diagram (c) for the different  $SU(2)_L$  models. An overall normalization factor, which includes the loop function and couplings, is not presented.

Model Operator	I	II	III	IV	V	VI	VII
$Q_{\ell q}^{(1)}$	3/4	1	0	3/4	9/8	0	3/4
$Q_{\ell q}^{(3)}$	-1/4	0	1/2	-1/4	1/8	1/2	1/2

Table III. Particle content and SM gauge representations for the scalar-rich (left) and fermion-rich (right) benchmark models.

	Scalar-Rich Model					Fermion-Rich Model			
	$\Psi$	$S_1$	$S_2$	$S_3$	$S_4$	$\Psi_1$	$S$	$\Psi_2$	$\Psi_3$
$SU(3)_c$	1	$\bar{3}$	1	$\bar{3}$	1	3	1	1	3
$SU(2)_L$	1	1	2	2	2	1	1	2	2
$Y$	$\alpha$	$\alpha + \frac{1}{3}$	$\alpha - \frac{1}{2}$	$\alpha - \frac{1}{6}$	$\alpha + \frac{1}{2}$	$\alpha$	$\alpha + \frac{1}{3}$	$\alpha - \frac{1}{6}$	$\alpha + \frac{1}{2}$

Applying these criteria to our classification allows us to identify potential DM candidates among the internal fields of each model. For any given model, we can examine if setting the free hypercharge parameter to a specific value renders one of the new particles a viable candidate. For instance, in model A-I of diagram (c), the internal fermion  $\Psi_1$  is a color singlet. By setting its hypercharge parameter  $\alpha = 0$ , it becomes electrically neutral ( $T_3 = 0, Y = 0$ ) and thus satisfies our primary conditions for a DM candidate. If a model contains multiple such candidates, the lightest one is assumed to be the stable DM particle.

### III. TWO BENCHMARK MODELS

As established in Sec. I, a viable explanation for the observed ratio  $\mathcal{B}(B^0 \rightarrow K^{*0} \nu \bar{\nu})/\mathcal{B}(B^+ \rightarrow K^+ \nu \bar{\nu})$ , which deviates from the SM prediction, necessitates the simultaneous generation of both  $\mathcal{O}_V^L$  and  $\mathcal{O}_V^R$ . Our classification in Sec. II provides a clear pathway to achieving this. We established that diagrams (c) and (d) can individually source both operator chiralities, while diagrams (a)/(b) and (e)/(f) form complementary pairs that generate  $\mathcal{O}_V^R$  and  $\mathcal{O}_V^L$ , respectively. While a simple combination of any two such valid models could suffice, this approach is often unappealing as it often introduces a large number of new particles. We therefore impose an additional criterion of minimality, seeking the most parsimonious models that can accomplish the task.

By systematically surveying all valid model combinations, we have identified two particularly economical scenarios. The most minimal model, containing only four new fields, arises from combining two distinct solutions derived from diagram (c). A second competitive scenario, containing five new fields, can be constructed by combining a model from diagram (a) with one from diagram (e). All other combinations result in models with six or more new degrees of freedom and are not considered further in this work.

Based on this analysis, we select two benchmark models for detailed study, whose particle content and SM gauge representations are defined in Table III. The first, which we term the “scalar-rich model”, is notable for its primarily scalar content. The second, termed the “fermion-rich model”, is instead dominated by new fermionic degrees of freedom.

We first consider the scalar-rich model. This benchmark model is constructed from a combination of diagram (a), which generates  $\mathcal{O}_V^R$ , and diagram (e), which generates  $\mathcal{O}_V^L$ . To make the model minimal, we identify the internal fermion in both diagrams as a single field,  $\Psi$ , while the four scalars are treated as distinct fields, relabeled  $S_{1..4}$ . The relevant interaction Lagrangian is

$$\begin{aligned} \mathcal{L} &\supset g_1^i \bar{\Psi} P_R d_i S_1 + g_2^i \bar{\Psi} P_R L_i^c S_2 + g_1^i \bar{\Psi} P_L Q_i S_3 + g_2^i \bar{\Psi} P_L L_i S_4 + \text{h.c.} \\ &= g_1^i \bar{\Psi} P_R d_i S_1 + g_2^i \bar{\Psi} P_R L_{i\alpha}^c S_{2\alpha} + g_1^i \bar{\Psi} P_L Q_{i\alpha} S_{3\beta} \epsilon_{\alpha\beta} + g_2^i \bar{\Psi} P_L L_{i\alpha} S_{4\beta} \epsilon_{\alpha\beta} + \text{h.c.} \end{aligned} \quad (8)$$

where  $i$  is a generation index,  $L_i^c$  represents the charge conjugate of the lepton doublet  $L_i$ , and  $\alpha, \beta$  are  $SU(2)_L$  indices contracted trivially (diagonally) or via the totally antisymmetric tensor  $\epsilon_{\alpha\beta}$ .

This model exhibits a special behavior when the hypercharge parameter  $\alpha = 0$ , which allows  $\Psi$  to be a Majorana fermion.

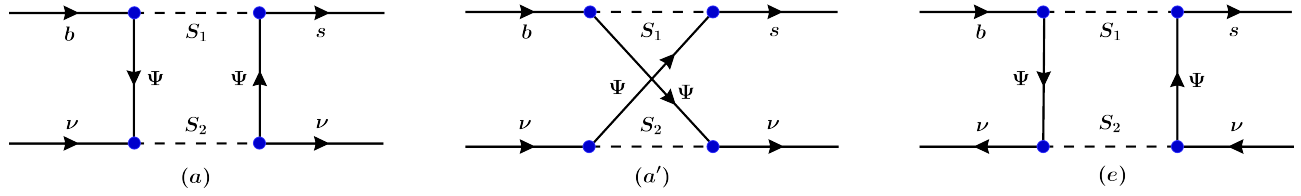


Figure 4. Illustration of the new diagrammatic contribution that becomes possible in the scalar-rich model when the mediating  $\Psi$  is a Majorana particle. The box diagram (a) is now accompanied by a “crossed” diagram, denoted (a'), where the internal fermion lines are exchanged. Note that this crossed diagram is topologically equivalent to the diagram (e).

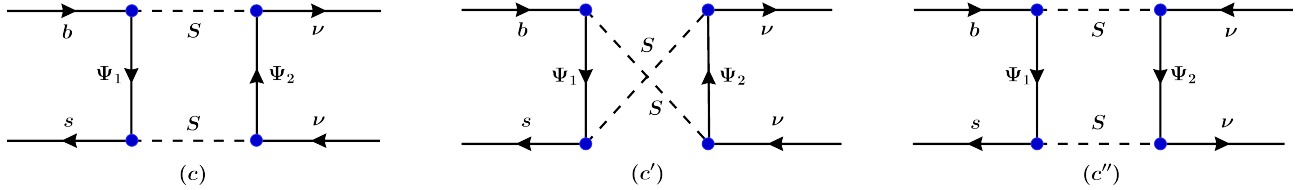


Figure 5. Illustration of additional diagrammatic contributions in the fermion-rich model that arise when the scalar mediator  $S$  is a real field. The box diagram (c) is accompanied by a “crossed-scalar” diagram (c'). This crossed diagram can be topologically rearranged to show its equivalence with diagram (c''), which is itself identical to the box diagram (d).

This possibility enables new “crossed” diagrams. As shown in Fig. 4, crossing the internal fermion lines of diagram (a) produces a new diagram (a'), which is topologically identical to diagram (e). Similarly, the crossed version of diagram (e) is equivalent to the diagram (a) in topology. Consequently, the Majorana nature of  $\Psi$  provides an additional mechanism for generating the required operators from the same fundamental Lagrangian.

Integrating out the new degrees of freedom yields the effective Lagrangian,

$$\mathcal{L}_{\text{eff}} = [C_{\ell q}^{(1)}]_{mnji} Q_{\ell q}^{(1)} + [C_{\ell d}]_{mnji} Q_{\ell d}, \quad (9)$$

with the Wilson coefficients given by

$$\begin{aligned} [C_{\ell d}]_{mnji} = & -\frac{(g_1^i g_1^{j*} g_2^m g_2^{n*})}{4} [J_4(m_{S_1}, m_{S_2}, m_{\Psi}, m_{\Psi}) + 2\eta^M m_{\Psi}^2 I_4(m_{S_1}, m_{S_2}, m_{\Psi}, m_{\Psi})] \\ & -\frac{(g_1^i g_1^{j*} g_2^n g_2^{m*})}{4} [2m_{\Psi}^2 I_4(m_{S_1}, m_{S_4}, m_{\Psi}, m_{\Psi}) + \eta^M J_4(m_{S_1}, m_{S_4}, m_{\Psi}, m_{\Psi})], \end{aligned} \quad (10)$$

$$\begin{aligned} [C_{\ell q}^{(1)}]_{mnji} = & \frac{(g_1^i g_1^{j*} g_2^n g_2^{m*})}{4} [J_4(m_{S_3}, m_{S_4}, m_{\Psi}, m_{\Psi}) + 2\eta^M m_{\Psi}^2 I_4(m_{S_3}, m_{S_4}, m_{\Psi}, m_{\Psi})] \\ & + \frac{g_1^i g_1^{j*} g_2^m g_2^{n*}}{4} [2m_{\Psi}^2 I_4(m_{S_2}, m_{S_3}, m_{\Psi}, m_{\Psi}) + \eta^M J_4(m_{S_2}, m_{S_3}, m_{\Psi}, m_{\Psi})]. \end{aligned} \quad (11)$$

Here, the factor  $\eta^M = 1$  parameterizes the additional contributions from a Majorana fermion  $\Psi$  (for which  $\eta^M = 0$ , they are absent), and  $I_4$  is a corresponding new loop function defined in Appendix A.

We now move on to the fermion-rich model, which is constructed by unifying two distinct solutions from diagram (c) to generate both  $\mathcal{O}_V^L$  and  $\mathcal{O}_V^R$ . To achieve this minimal spectrum, we postulate that the internal scalar is a single field,  $S$ , common to both solutions, and that one of the internal fermions is also common to both, which we label  $\Psi_2$ . The remaining two fermions are distinct fields, denoted as  $\Psi_1$  and  $\Psi_3$ . This specific combination of fields leads to the following interaction Lagrangian:

$$\begin{aligned} \mathcal{L} = & g_1^i \bar{\Psi}_1 P_R d_i S + g_2^i \bar{L}^i P_R \Psi_2 S^\dagger + g_1^i \bar{\Psi}_3 P_L Q_i S + \text{h.c.} \\ = & g_1^i \bar{\Psi}_1 P_R d_i S + g_2^i \bar{L}_\alpha^i P_R \Psi_{2\alpha} S^\dagger + g_1^i \bar{\Psi}_{3\alpha} P_L Q_{i\alpha} S + \text{h.c.}, \end{aligned} \quad (12)$$

where  $i$  denotes the generation index and  $\alpha$  is the  $SU(2)_L$  index.

As in the scalar-rich case, the possibility of the scalar  $S$  being a real field (i.e.,  $\alpha = -1/3$ ) allows for contributions from “crossed-scalar” diagrams. As illustrated in Fig. 5, the box diagram (c) is now accompanied by a crossed diagram (c'), where the internal scalar lines are exchanged. This new diagram (c') can be topologically rearranged to show its equivalence with the diagram (d), via the intermediate form (c'').

Integrating out the new particles in the fermion-rich model yields the same operator structure as in Eq. (9), but with Wilson coefficients that depend critically on whether the scalar  $S$  is real or complex. If  $S$  is real, a cancellation occurs between the standard and “crossed-scalar” diagrams. We parameterize this with a factor  $\eta^M$ , set to 1 for a real scalar and 0 for a complex one, which leads to the coefficients

$$[C_{\ell d}]_{mnji} = \frac{(g_1^i g_1^{j*} g_2^m g_2^{n*})}{4} J_4(m_{\Psi_1}, m_{\Psi_2}, m_S, m_S) (1 - \eta^M), \quad (13)$$

$$[C_{\ell q}^{(1)}]_{mnji} = \frac{(g_1^i g_1^{j*} g_2^m g_2^{n*})}{4} J_4(m_{\Psi_2}, m_{\Psi_3}, m_S, m_S) (1 - \eta^M). \quad (14)$$

Evidently, both coefficients vanish for a real scalar mediator, a result consistent with the findings of Ref. [66].

#### IV. OBSERVABLES AND CONSTRAINTS ON WILSON COEFFICIENTS

In the previous section, we constructed two benchmark models—a scalar-rich and a fermion-rich scenario—to address the anomaly associated with the ratio  $\mathcal{B}(B^0 \rightarrow K^{*0} \nu \bar{\nu})/\mathcal{B}(B^+ \rightarrow K^+ \nu \bar{\nu})$  through one-loop contributions. The viability of these models depends on their respective sets of free parameters (couplings and masses), which we will analyze under the simplifying assumption that they only couple to third-generation neutrinos. However, the Lagrangians that generate the desired  $b \rightarrow s \nu \bar{\nu}$  operators will inevitably source other FCNC processes. These include contributions to  $B_s \rightarrow \tau^+ \tau^-$ ,  $B \rightarrow K \tau^+ \tau^-$ ,  $B_s - \bar{B}_s$  mixing,  $B$  meson radiative decays, and  $Z$  boson decays, all of which are subject to experimental constraints. A complete phenomenological analysis is therefore required to determine the allowed parameter space of our models. To this end, we will proceed in this section by first calculating the Wilson coefficients for all relevant constraining processes. Subsequently, we will use the current experimental data for these observables to derive bounds on the new particles’ masses and couplings.

##### A. $B \rightarrow K^{(*)} \nu \bar{\nu}$

We begin by establishing the LEFT operators for  $b \rightarrow s \nu_\ell \bar{\nu}_\ell$  transitions. Under the assumptions that right-handed neutrinos are absent, all neutrinos are Dirac, and lepton flavor is conserved, the most general effective Lagrangian is

$$\mathcal{L}_{\text{eff}} = \frac{8G_F}{\sqrt{2}} V_{tb} V_{ts}^* \frac{\alpha}{4\pi} \sum_{\ell=e,\mu,\tau} (C_L^{\nu_\ell} \mathcal{O}_V^L + C_R^{\nu_\ell} \mathcal{O}_V^R) + \text{h.c.}, \quad (15)$$

where  $G_F$  is the Fermi constant,  $\alpha$  is the fine-structure constant, and  $V_{ij}$  denote the CKM matrix elements. The operators  $\mathcal{O}_V^{L,R}$  are defined in Eq. (1). In the SM, the right-handed current is absent ( $C_{R,\text{SM}}^{\nu_\ell} = 0$ ), while the left-handed Wilson coefficient is predicted to be  $C_{L,\text{SM}}^{\nu_\ell} = -6.32(7)$  [39, 67, 68]. We parameterize NP contributions as shifts to these coefficients, denoted by  $\Delta C_{L,R}^{\nu_\ell}$ .

To connect our high-scale models to this framework, we match the SMEFT Wilson coefficients onto the LEFT basis at the electroweak scale. Neglecting the small RG running effects, the tree-level matching relations for the relevant operators are

$$\Delta C_L^{\nu_\ell} = \frac{\pi}{\sqrt{2}\alpha G_F V_{tb} V_{ts}^*} [C_{\ell q}^{(1)}]_{\ell\ell 23}, \quad (16)$$

$$\Delta C_R^{\nu_\ell} = \frac{\pi}{\sqrt{2}\alpha G_F V_{tb} V_{ts}^*} [C_{\ell d}]_{\ell\ell 23}. \quad (17)$$

The branching ratios for the decays  $B \rightarrow K^{(*)} \nu \bar{\nu}$  can be expressed numerically in terms of these Wilson coefficients. Adopting the form factors from Refs. [2, 67], the theoretical predictions are given by [42]

$$\mathcal{B}(B^+ \rightarrow K^+ \nu \bar{\nu}) = 3.46 \times 10^{-8} \sum_{\ell=e,\mu,\tau} |C_L^{\nu_\ell} + C_R^{\nu_\ell}|^2, \quad (18)$$

$$\mathcal{B}(B^0 \rightarrow K^{*0} \nu \bar{\nu}) = 6.84 \times 10^{-8} \sum_{\ell=e,\mu,\tau} |C_L^{\nu_\ell} - C_R^{\nu_\ell}|^2 + 1.36 \times 10^{-8} \sum_{\ell=e,\mu,\tau} |C_L^{\nu_\ell} + C_R^{\nu_\ell}|^2, \quad (19)$$

where  $C_{L(R)}^{\nu_\ell} = C_{L(R),\text{SM}}^{\nu_\ell} + \Delta C_{L(R)}^{\nu_\ell}$ .

These predictions are confronted with experimental data, including the Belle II measurement  $\mathcal{B}(B^+ \rightarrow K^+ \nu \bar{\nu})_{\text{exp}} = (2.3 \pm 0.7) \times 10^{-5}$  [1] and the Belle limit  $\mathcal{B}(B^0 \rightarrow K^{*0} \nu \bar{\nu})_{\text{exp}} < 1.8 \times 10^{-5}$  at 90% confidence level (C.L.) [3]. In the simplified

scenario where NP couples exclusively to the third lepton generation (i.e.,  $\Delta C_{L,R}^{\nu_{e,\mu}} = 0$ ), we derive the following constraints on the NP contributions:

$$|\Delta C_L^{\nu_\tau} - 6.32 + \Delta C_R^{\nu_\tau}|^2 \leq 5.85 \times 10^2, \quad (20)$$

$$1.5 \left( |\Delta C_L^{\nu_\tau} - 6.32|^2 + |\Delta C_R^{\nu_\tau}|^2 \right) - 2\text{Re}[(\Delta C_L^{\nu_\tau} - 6.32)\Delta C_R^{\nu_\tau*}] \leq 2.09 \times 10^2. \quad (21)$$

### B. $b \rightarrow s\tau^+\tau^-$

The next set of constraints arises from  $b \rightarrow s\tau^+\tau^-$  transitions, described by the low-energy effective Lagrangian

$$\mathcal{L}_{\text{eff}} = \frac{4G_F}{\sqrt{2}} V_{tb} V_{ts}^* \frac{\alpha}{4\pi} \sum_{i=9,10} (C_i \mathcal{O}_i + C'_i \mathcal{O}'_i) + \text{h.c.}, \quad (22)$$

with the four-fermion operators defined as

$$\mathcal{O}_9^{(\prime)} = (\bar{s}\gamma_\mu P_{L(R)} b)(\bar{\tau}\gamma^\mu \tau), \quad \mathcal{O}_{10}^{(\prime)} = (\bar{s}\gamma_\mu P_{L(R)} b)(\bar{\tau}\gamma^\mu \gamma_5 \tau). \quad (23)$$

In the SM, only the unprimed operators are generated, with Wilson coefficients evaluated at the scale  $\mu_b = 4.2$  GeV to be  $C_{9,\text{SM}} \approx 4.11$  and  $C_{10,\text{SM}} \approx -4.19$  at next-to-next-to-leading logarithmic order [69].

In general, NP contributions to these operators can originate from box,  $Z$ -penguin, and photon-penguin diagrams. However, for the class of models considered here, the box contributions dominate. Since our models do not introduce new sources of SU(2) breaking,  $Z$ -penguin diagrams are suppressed by factors of  $m_b^2/M_Z^2$ . Similarly, photon-penguin contributions to  $C_9$  are strongly constrained by  $b \rightarrow s\gamma$  and  $B_s - \bar{B}_s$  mixing data and are subdominant in the parameter space of interest [66]. Focusing therefore on the dominant box diagrams, we match the generated SMEFT operators  $Q_{\ell q}^{(1)}$  and  $Q_{\ell d}$  onto the LEFT basis, yielding the relations:

$$\Delta C_9 = -\Delta C_{10} = \frac{\pi}{\sqrt{2}\alpha G_F V_{tb} V_{ts}^*} [C_{\ell q}^{(1)}]_{3323}, \quad (24)$$

$$\Delta C'_9 = -\Delta C'_{10} = \frac{\pi}{\sqrt{2}\alpha G_F V_{tb} V_{ts}^*} [C_{\ell d}]_{3323}. \quad (25)$$

The effective Lagrangian in Eq. (22) can mediate the rare decay  $B_s \rightarrow \tau^+\tau^-$ , providing a direct constraint on the Wilson coefficients  $C_{10}^{(\prime)}$ . The branching ratio is given by

$$\mathcal{B}(B_s \rightarrow \tau^+\tau^-) = \tau_{B_s} \frac{G_F^2 \alpha^2}{16\pi^3} |V_{ts} V_{tb}^*|^2 f_{B_s}^2 m_{B_s} m_\tau^2 \sqrt{1 - \frac{4m_\tau^2}{m_{B_s}^2}} |C_{10} - C'_{10}|^2, \quad (26)$$

where  $C_{10}^{(\prime)} = C_{10,\text{SM}}^{(\prime)} + \Delta C_{10}^{(\prime)}$ . Note that the vector operators  $\mathcal{O}_9^{(\prime)}$  do not contribute to this purely leptonic final state due to parity conservation in the hadronic matrix element. The current experimental constraint is an upper limit set by the LHCb collaboration,  $\mathcal{B}(B_s \rightarrow \tau^+\tau^-)_{\text{exp}} < 6.8 \times 10^{-3}$  at 95% C.L. [70]. Imposing this bound on the theoretical prediction yields the constraint:

$$|\Delta C_{10} - \Delta C'_{10}|^2 \leq 3.71 \times 10^3. \quad (27)$$

While this constraint is currently loose, the sensitivity is expected to improve in the coming years. Future LHCb upgrades project a limit of approximately  $5 \times 10^{-4}$  [71], and future colliders such as the Circular Electron Positron Collider (CEPC) could potentially reach sensitivities of order  $10^{-5}$  [72].

Finally, we examine the semi-leptonic decay  $\bar{B} \rightarrow K\tau^+\tau^-$ . The differential decay rate with respect to the dilepton invariant mass squared  $s \equiv q^2$  is given by [73]:

$$\begin{aligned} \frac{d\Gamma(\bar{B} \rightarrow K\tau^+\tau^-)}{ds} = & 2\Gamma_0 \lambda^{1/2}(M_B^2, M_K^2, s) \beta_\tau \left\{ s|F_P|^2 + \frac{1}{6} \lambda(M_B^2, M_K^2, s) \left( 1 + \frac{2m_\tau^2}{s} \right) (|F_A|^2 + |F_V|^2) \right. \\ & \left. + 4m_\tau^2 M_B^2 |F_A|^2 + 2m_\tau(M_B^2 - M_K^2 + s) \text{Re}(F_P F_A^*) \right\}, \end{aligned} \quad (28)$$

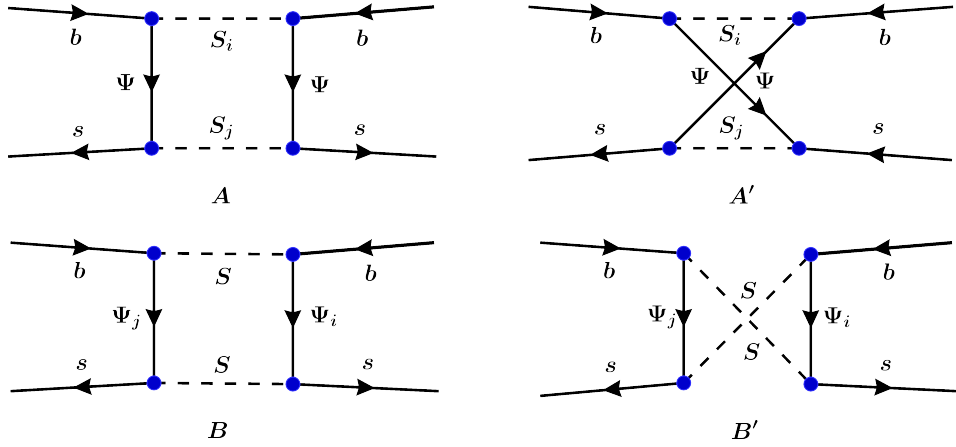


Figure 6. One-loop diagrams contributing to  $B_s - \bar{B}_s$  mixing. The top panel shows diagrams for the scalar-rich model, where the standard box (A) is accompanied by a ‘crossed-fermion’ diagram (A') if the mediator  $\Psi$  is a Majorana particle. The bottom panel shows diagrams for the fermion-rich model, where the standard box (B) is accompanied by a ‘crossed-scalar’ diagram (B') if the mediator  $S$  is a real scalar. The indices  $i, j$  on the mediators correspond to the distinct particle species defined in each model.

where the kinematic range is  $4m_\tau^2 \leq s \leq (M_B - M_K)^2$ . The normalization factor and kinematic functions are defined as

$$\Gamma_0 = \frac{G_F^2 \alpha^2}{2^9 \pi^5 M_B^3} |V_{tb} V_{ts}^*|^2, \quad \beta_\tau = \sqrt{1 - 4m_\tau^2/s}, \quad \lambda(a, b, c) = a^2 + b^2 + c^2 - 2(ab + bc + ac). \quad (29)$$

The dynamical functions  $F_{P,A,V}$  incorporate contributions from both unprimed and primed operators:

$$\begin{aligned} F_P &= -m_\tau (C_{10} + C'_{10}) \left[ f_+(s) - \frac{M_B^2 - M_K^2}{s} (f_0(s) - f_+(s)) \right], \\ F_A &= (C_{10} + C'_{10}) f_+(s), \\ F_V &= (C_9 + C'_9) f_+(s), \end{aligned} \quad (30)$$

where we adopt the vector ( $f_+$ ) and scalar ( $f_0$ ) form factors from Ref. [2]. Integrating this rate over the allowed kinematic region and applying the BaBar upper limit  $\mathcal{B}(B^+ \rightarrow K^+ \tau^+ \tau^-) \leq 2.25 \times 10^{-3}$  (90% C.L.) [74], we obtain the following numerical constraint on the NP contributions (employing the relations in Eqs. (24) and (25)):

$$\begin{aligned} &\left[ 1.56 \times 10^{-7} + 1.50 \times 10^{-23} (\Delta C_9 + \Delta C'_9) + 8.93 \times 10^{-9} (\Delta C_9 + \Delta C'_9) (\Delta C_9^* + \Delta C'^*_9) \right. \\ &\quad \left. + 7.47 \times 10^{-8} \text{Re}(\Delta C_9 + \Delta C'_9) \right] \leq 2.25 \times 10^{-3}. \end{aligned} \quad (31)$$

### C. $B_s - \bar{B}_s$ mixing

Another set of constraints on our models arises from their potential contributions to  $B_s - \bar{B}_s$  mixing. At low energies, this process is described by the effective Hamiltonian

$$\mathcal{H}_{\text{eff}} = \sum_a C_a \mathcal{O}_a + \text{h.c.} \quad (32)$$

Adopting the so-called BMU basis [75], the relevant operators for our analysis are listed as follows:

$$\mathcal{O}_{\text{VLL}} = (\bar{s} \gamma_\mu P_L b)(\bar{s} \gamma^\mu P_L b), \quad \mathcal{O}_{\text{VRR}} = (\bar{s} \gamma_\mu P_R b)(\bar{s} \gamma^\mu P_R b), \quad \mathcal{O}_{\text{LR},1} = (\bar{s} \gamma_\mu P_L b)(\bar{s} \gamma^\mu P_R b). \quad (33)$$

While the SM contribution to this process is dominated by  $\mathcal{O}_{VLL}$ , its effect is CKM-suppressed and can be safely neglected [76]. In the SMEFT framework, our benchmark models generate contributions to three of the primary  $\Delta B = 2$  operators, namely

$$Q_{qq}^{(1)} = (\bar{Q}_2 \gamma^\mu Q_3) (\bar{Q}_2 \gamma^\mu Q_3) , \quad (34)$$

$$Q_{qd}^{(1)} = (\bar{Q}_2 \gamma^\mu Q_3) (\bar{d}_{R,2} \gamma^\mu d_{R,3}) , \quad (35)$$

$$Q_{dd} = (\bar{d}_{R,2} \gamma^\mu d_{R,3}) (\bar{d}_{R,2} \gamma^\mu d_{R,3}) , \quad (36)$$

where the subscript denotes the generation of quark fields. The tree-level matching between the SMEFT and LEFT at the electroweak scale yields a direct correspondence between the Wilson coefficients of these operators:

$$\begin{aligned} C_{VLL} &= [C_{qq}^{(1)}]_{2323} , \\ C_{VRR} &= [C_{dd}]_{2323} , \\ C_{LR,1} &= [C_{qd}^{(1)}]_{2323} . \end{aligned} \quad (37)$$

The one-loop box diagrams that generate these SMEFT operators in our benchmark models are depicted in Fig. 6. As in the previous sections, the contributions depend on whether the mediating particles are complex or real. For the scalar-rich model, where the fermion  $\Psi$  can be a Majorana particle ( $\eta^M = 1$ ), we obtain

$$[C_{qd}^{(1)}]_{2323} = \frac{(g_1^3 g_1^{2*} g_{1'}^3 g_{1'}^{2*})}{4} \left[ 2m_\Psi^2 I_4(m_{S_1}, m_{S_3}, m_\Psi, m_\Psi) + \eta^M J_4(m_{S_1}, m_{S_3}, m_\Psi, m_\Psi) \right] , \quad (38)$$

$$[C_{dd}]_{2323} = -\frac{(g_1^3 g_1^{2*})^2}{8} \left[ J_4(m_{S_1}, m_{S_1}, m_\Psi, m_\Psi) + 2\eta^M m_\Psi^2 I_4(m_{S_1}, m_{S_1}, m_\Psi, m_\Psi) \right] , \quad (39)$$

$$[C_{qq}^{(1)}]_{2323} = -\frac{(g_1^3 g_{1'}^{2*})^2}{8} \left[ J_4(m_{S_3}, m_{S_3}, m_\Psi, m_\Psi) + 2\eta^M m_\Psi^2 I_4(m_{S_3}, m_{S_3}, m_\Psi, m_\Psi) \right] . \quad (40)$$

In the fermion-rich model, where the scalar  $S$  can be real ( $\eta^M = 1$ ), we find a cancellation between the standard and crossed-box diagrams, leading to

$$[C_{dd}]_{2323} = -\frac{(g_1^3 g_1^{2*})^2}{8} J_4(m_S, m_S, m_{\Psi_1}, m_{\Psi_1})(1 - \eta^M) , \quad (41)$$

$$[C_{qq}^{(1)}]_{2323} = -\frac{(g_1^3 g_{1'}^{2*})^2}{8} J_4(m_S, m_S, m_{\Psi_3}, m_{\Psi_3})(1 - \eta^M) , \quad (42)$$

$$[C_{qd}^{(1)}]_{2323} = -\frac{(g_1^3 g_1^{2*} g_{1'}^3 g_{1'}^{2*})}{4} J_4(m_S, m_S, m_{\Psi_1}, m_{\Psi_3})(1 - \eta^M) . \quad (43)$$

In both sets of equations,  $\eta^M = 0$  if the particle is complex (Dirac fermion or complex scalar) and  $\eta^M = 1$  otherwise.

The theoretical prediction for the  $B_s - \bar{B}_s$  mass difference,  $\Delta M_s$ , is determined by the off-diagonal element of the mass matrix,  $\Delta M_s = 2|M_{12}|$ . This matrix element is calculated from the effective Hamiltonian in Eq. (32) via

$$M_{12} = \frac{\langle B_s | \mathcal{H}_{\text{eff}} | \bar{B}_s \rangle}{2M_{B_s}} = \frac{1}{2M_{B_s}} \sum_a C_a(\mu) \langle \mathcal{O}_a \rangle(\mu) , \quad (44)$$

where  $\langle \mathcal{O}_a \rangle(\mu) \equiv \langle B_s | \mathcal{O}_a | \bar{B}_s \rangle(\mu)$  denote the hadronic matrix elements of the operators evaluated at the scale  $\mu$ . Although both the Wilson coefficients  $C_a(\mu)$  and the matrix elements  $\langle \mathcal{O}_a \rangle(\mu)$  are dependent on the renormalization scale  $\mu$ , the physical observable  $\Delta M_s$  is scale-independent.

We confront these predictions with the precise measurement from the LHCb collaboration,  $\Delta M_s = (1.1693 \pm 0.0004) \times 10^{-8} \text{ MeV}$  [77]. For the theoretical inputs, we adopt the matrix elements calculated in the  $\overline{\text{MS}}\text{-NDR}$  scheme at  $\mu = 4.16 \text{ GeV}$  [76]:

$$\langle \mathcal{O}_{VLL} \rangle = \langle \mathcal{O}_{VRR} \rangle = 0.86 \text{ GeV}^4 , \quad \langle \mathcal{O}_{LR,1} \rangle = -1.48 \text{ GeV}^4 . \quad (45)$$

Inserting these values into Eq. (44), we derive the following constraint on the NP Wilson coefficients:

$$\frac{1}{M_{B_s}} |0.86(C_{VLL} + C_{VRR}) - 1.48C_{LR,1}| \leq 1.1693 \times 10^{-11} \text{ GeV} . \quad (46)$$

This inequality, combined with the matching conditions in Eq. (37), directly constrains the parameter space of our benchmark models.

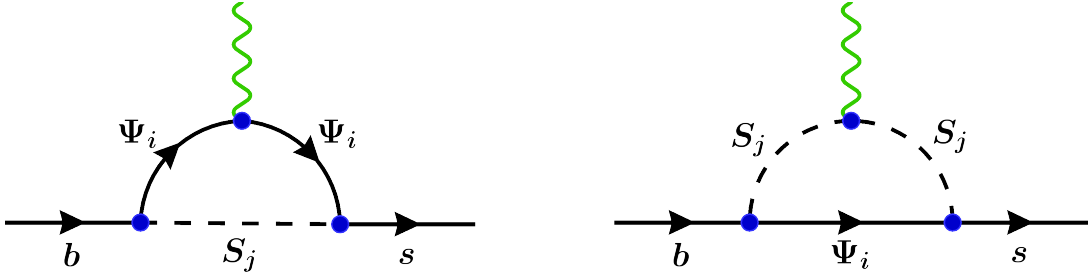


Figure 7. One-loop contributions to  $b \rightarrow s\gamma$  in the benchmark models. Replacing the photon (wavy green line) with a gluon yields the corresponding diagrams for the chromomagnetic transition  $b \rightarrow sg$ .

#### D. $b \rightarrow s\gamma$

The radiative dipole transition  $b \rightarrow s\gamma$  also provides stringent constraints on our models. This process is described by the effective Hamiltonian

$$\mathcal{H}_{\text{eff}} = -\frac{4G_F}{\sqrt{2}} V_{tb} V_{ts}^* \sum_{i=7,8} (C_i \mathcal{O}_i + C'_i \mathcal{O}'_i), \quad (47)$$

which contains the electromagnetic and chromomagnetic dipole operators:

$$\begin{aligned} \mathcal{O}_7 &= \frac{e}{16\pi^2} m_b \bar{s} \sigma^{\mu\nu} P_R b F_{\mu\nu}, & \mathcal{O}_8 &= \frac{g_s}{16\pi^2} m_b \bar{s}_\alpha \sigma^{\mu\nu} P_R T_{\alpha\beta}^a b_\beta G_{\mu\nu}^a, \\ \mathcal{O}'_7 &= \frac{e}{16\pi^2} m_b \bar{s} \sigma^{\mu\nu} P_L b F_{\mu\nu}, & \mathcal{O}'_8 &= \frac{g_s}{16\pi^2} m_b \bar{s}_\alpha \sigma^{\mu\nu} P_L T_{\alpha\beta}^a b_\beta G_{\mu\nu}^a. \end{aligned} \quad (48)$$

Here,  $F_{\mu\nu}$  and  $G_{\mu\nu}^a$  are the electromagnetic and gluonic field strength tensors, respectively. The process  $b \rightarrow s\gamma$  is directly governed by the Wilson coefficients  $C_7^{(\prime)}$ , which also receive contributions from the QCD mixing of the  $C_8^{(\prime)}$  coefficients.

In our benchmark models, these operators are generated at the one-loop level through the diagrams shown in Fig. 7. We now calculate the new physics contributions to the Wilson coefficients, denoted as  $\Delta C_{7,8}^{(\prime)}$ , for each of our two models in turn.

First, we consider the scalar-rich model. In this scenario, the mediating fermion is always the color-singlet  $\Psi$ , while the internal scalars can be either  $S_1$  or  $S_3$ , both of which are color anti-triplets. Integrating out these heavy particles yields the following NP contributions to the electromagnetic dipole coefficients:

$$\Delta C_7 = -\frac{g_1^3 g_1^{2*}}{2m_{S_1}^2} \frac{m_s}{m_b} \left( Q_{S_1} \tilde{F}_7(x_1) + Q_\Psi F_7(x_1) \right) - \frac{g_{1'}^3 g_{1'}^{2*}}{2m_{S_3}^2} \left( Q_{S_3} \tilde{F}_7(x_3) + Q_\Psi F_7(x_3) \right), \quad (49)$$

$$\Delta C'_7 = -\frac{g_1^3 g_1^{2*}}{2m_{S_1}^2} \left( Q_{S_1} \tilde{F}_7(x_1) + Q_\Psi F_7(x_1) \right) - \frac{g_{1'}^3 g_{1'}^{2*}}{2m_{S_3}^2} \frac{m_s}{m_b} \left( Q_{S_3} \tilde{F}_7(x_3) + Q_\Psi F_7(x_3) \right), \quad (50)$$

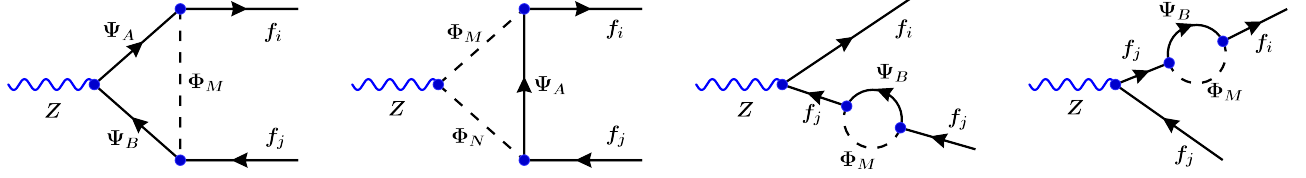
where the mass ratios are defined as  $x_j = m_\Psi^2/m_{S_j}^2$  for  $j = 1, 3$ , and the loop functions  $F_7$  and  $\tilde{F}_7$  are given in Appendix A. The contributions to the chromomagnetic coefficients,  $\Delta C_8^{(\prime)}$ , are obtained by replacing the electric charges  $Q_X$  with color factors  $\chi_X$ . In this case,  $\chi_\Psi = 0$  for the color singlet  $\Psi$ , while  $\chi_{S_{1,3}} = 1$  for the color anti-triplets  $S_{1,3}$ .

Next, we analyze the fermion-rich model. Here, the mediating scalar  $S$  is a color singlet, while the internal fermions can be either  $\Psi_1$  or  $\Psi_3$ , both color triplets. The resulting NP contributions are

$$\Delta C_7 = -\frac{g_1^3 g_1^{2*}}{2m_S^2} \frac{m_s}{m_b} \left( Q_S \tilde{F}_7(x_1) + Q_{\Psi_1} F_7(x_1) \right) - \frac{g_{1'}^3 g_{1'}^{2*}}{2m_S^2} \left( Q_S \tilde{F}_7(x_3) + Q_{\Psi_3} F_7(x_3) \right), \quad (51)$$

$$\Delta C'_7 = -\frac{g_1^3 g_1^{2*}}{2m_S^2} \left( Q_S \tilde{F}_7(x_1) + Q_{\Psi_1} F_7(x_1) \right) - \frac{g_{1'}^3 g_{1'}^{2*}}{2m_S^2} \frac{m_s}{m_b} \left( Q_S \tilde{F}_7(x_3) + Q_{\Psi_3} F_7(x_3) \right), \quad (52)$$

where the mass ratios are now defined as  $x_j = m_{\Psi_j}^2/m_S^2$ . The corresponding chromomagnetic coefficients  $\Delta C_8^{(\prime)}$  are again found by substituting electric charges with color factors. Specifically,  $\chi_S = 0$  for the color scalar  $S$  and  $\chi_{\Psi_{1,3}} = 1$  for the color triplets  $\Psi_{1,3}$ .

Figure 8. Feynman diagrams modifying the  $Z\bar{f}_i f_j$  vertex with  $f_{i,j} \in \{s, b, \ell, \nu\}$ .

The theoretical prediction for the branching ratio, including the photon energy cut  $E_\gamma > E_0 = 1.6$  GeV, can be separated into the SM prediction and the NP correction:

$$\bar{\mathcal{B}}(b \rightarrow s\gamma) = \bar{\mathcal{B}}(b \rightarrow s\gamma)^{\text{SM}} + \delta\bar{\mathcal{B}}(b \rightarrow s\gamma). \quad (53)$$

The NP contribution,  $\delta\bar{\mathcal{B}}(b \rightarrow s\gamma)$ , evaluated at scale  $\mu = 160$  GeV is given by [78, 79]

$$\begin{aligned} \delta\bar{\mathcal{B}}(b \rightarrow s\gamma) = & 10^{-4} \times \text{Re}[-8.100\Delta\mathcal{C}_7 - 2.509\Delta\mathcal{C}_8 + 2.767(\Delta\mathcal{C}_7\Delta\mathcal{C}_8^* + \Delta\mathcal{C}_7'\Delta\mathcal{C}_8'^*) \\ & + 5.348(|\Delta\mathcal{C}_7|^2 + |\Delta\mathcal{C}_7'|^2) + 0.890(|\Delta\mathcal{C}_8|^2 + |\Delta\mathcal{C}_8'|^2)]. \end{aligned} \quad (54)$$

For our analysis, we have only taken account of the contributions from the leading order of  $\Delta\mathcal{C}_{7,8}^{(\prime)}$ . For the complete next-to-leading order expression, we refer the reader to the original references.

The current world average for the experimental branching ratio is [80]:

$$\mathcal{B}(B \rightarrow X_s\gamma)^{\text{exp}} = (3.49 \pm 0.19) \times 10^{-4}, \quad (55)$$

compared to the SM prediction at the NNLO [81]:

$$\mathcal{B}(B \rightarrow X_s\gamma)^{\text{SM}} = (3.36 \pm 0.23) \times 10^{-4}. \quad (56)$$

The difference between the experimental value and the SM prediction provides a window for new physics. By requiring our calculated NP contribution,  $\delta\bar{\mathcal{B}}(b \rightarrow s\gamma)$ , to be consistent with this window, we can place a direct constraint on the NP Wilson coefficients  $\Delta\mathcal{C}_{7,8}^{(\prime)}$ .

### E. Impact on $Z\bar{f}f$ Couplings

Constraints also arise from radiative corrections to the effective  $Z$ -boson couplings to SM fermions. We consider contributions affecting both on-shell  $Z$  decay vertices and off-shell  $Z$  exchange amplitudes. With the detailed analytical expressions for the generic one-loop functions provided in Appendix B, we focus here on applying these results to the specific interaction structures of our two benchmark models.

For the scalar-rich model, the fermion sector contains a single  $SU(2)_L$  singlet, vector-like fermion  $\Psi$ . Its couplings to the  $Z$  boson, following the notation of Eq. (B4), are given by:

$$g^{\Psi,L} = g^{\Psi,R} = -\alpha s_W^2. \quad (57)$$

Regarding the scalar fields, we organize them into multiplets  $\Phi_M$  to match the generic formalism. We explicitly label their components by their electric charges (superscripts) and group them as follows:

$$\Phi_1 = \begin{pmatrix} S_1^{\alpha+\frac{1}{3}} \\ S_3^{\alpha+\frac{1}{3}} \end{pmatrix}, \quad \Phi_2 = \begin{pmatrix} S_2^\alpha \\ S_4^\alpha \end{pmatrix}, \quad \Phi_3 = S_2^{\alpha-1}, \quad \Phi_4 = S_4^{\alpha+1}. \quad (58)$$

The components of  $\Phi_1$  couple to down-type quarks  $d_i$ , and those of  $\Phi_2$  to left-handed neutrinos  $\nu_i$ . In addition,  $\Phi_4$  couples to the charged leptons  $e_i$ , while  $\Phi_3$  interacts with the corresponding charge-conjugated fields  $e_i^c$ . We omit the component  $S_3^{\alpha-2/3}$ , as it couples exclusively to up-type quarks. The corresponding  $Z$ -coupling matrices  $g^{\Phi_M}$  (cf. Eq. (B4)) are given by

$$\begin{aligned} g^{\Phi_1} &= \begin{pmatrix} -Q_{\Phi_1}s_W^2 & 0 \\ 0 & \frac{1}{2} - Q_{\Phi_1}s_W^2 \end{pmatrix}, & g^{\Phi_3} &= -\frac{1}{2} - Q_{\Phi_3}s_W^2, \\ g^{\Phi_2} &= \begin{pmatrix} \frac{1}{2} - Q_{\Phi_2}s_W^2 & 0 \\ 0 & -\frac{1}{2} - Q_{\Phi_2}s_W^2 \end{pmatrix}, & g^{\Phi_4} &= \frac{1}{2} - Q_{\Phi_4}s_W^2, \end{aligned} \quad (59)$$

where the relevant electric charges are  $Q_{\Phi_1} = \alpha + 1/3$ ,  $Q_{\Phi_2} = \alpha$ ,  $Q_{\Phi_3} = \alpha - 1$ , and  $Q_{\Phi_4} = \alpha + 1$ .

Turning to the fermion-rich model, the scalar sector consists of a single  $SU(2)_L$  singlet field  $S$ , with a  $Z$  boson coupling determined solely by its charge:

$$g^S = -\alpha s_W^2. \quad (60)$$

The vector-like fermion sector contains multiple fields. Labeling the fermion components by their electric charges, we define the multiplets  $F_{1,2,3}$  as:

$$F_1 = \begin{pmatrix} \Psi_1^\alpha \\ \Psi_3^\alpha \end{pmatrix}, \quad F_2 = \Psi_2^{\alpha+\frac{1}{3}}, \quad F_3 = \Psi_2^{\alpha-\frac{2}{3}}. \quad (61)$$

The component  $\Psi_3^{\alpha+1}$  is not presented, because it couples exclusively to up-type quarks. The corresponding  $Z$  couplings of the multiplets  $F_{1,2,3}$  (cf. Eq. (B4)) are given by

$$\begin{aligned} g^{F_1,L} = g^{F_1,R} &= \begin{pmatrix} -Q_{F_1} s_W^2 & 0 \\ 0 & -\frac{1}{2} - Q_{F_1} s_W^2 \end{pmatrix}, \\ g^{F_2,L} = g^{F_2,R} &= \frac{1}{2} - Q_{F_2} s_W^2, \\ g^{F_3,L} = g^{F_3,R} &= -\frac{1}{2} - Q_{F_3} s_W^2, \end{aligned} \quad (62)$$

where the relevant electric charges are  $Q_{F_1} = \alpha$ ,  $Q_{F_2} = \alpha + 1/3$ , and  $Q_{F_3} = \alpha - 2/3$ .

With the couplings and field components established, we proceed to calculate the one-loop corrections to the decay modes  $Z \rightarrow \bar{s}b$ ,  $\tau^+\tau^-$ , and  $\nu_\tau\bar{\nu}_\tau$ . In the scalar-rich model, the contributions to the effective couplings are found to be:

$$\Delta g_L^{sb}(m_Z^2) = \frac{m_Z^2}{32\pi^2} g_1^{2*} g_1^3 \left[ \frac{g^{\Psi,L}}{M_{S_3}^2} x_3 \tilde{G}_Z(x_3, x_3) - \frac{2}{3} \frac{g^{\Psi,R}}{M_{S_3}^2} \tilde{F}_Z(x_3, x_3) + \frac{(g^{\Phi_1})_{22}}{3M_\Psi^2} \tilde{H}_Z(x_3, x_3) \right], \quad (63)$$

$$\Delta g_R^{sb}(m_Z^2) = \frac{m_Z^2}{32\pi^2} g_1^{2*} g_1^3 \left[ \frac{g^{\Psi,R}}{M_{S_1}^2} x_1 \tilde{G}_Z(x_1, x_1) - \frac{2}{3} \frac{g^{\Psi,L}}{M_{S_1}^2} \tilde{F}_Z(x_1, x_1) + \frac{(g^{\Phi_1})_{11}}{3M_\Psi^2} \tilde{H}_Z(x_1, x_1) \right], \quad (64)$$

for the quark modes. For the leptonic modes, we must account for the color charge of the internal NP fields, which yields an enhancement factor of  $\chi_Z = 3$ . The resulting expressions are:

$$\begin{aligned} \Delta g_L^{\tau\tau}(m_Z^2) = & \frac{3m_Z^2}{32\pi^2} \left\{ |g_2^3|^2 \left[ \frac{g^{\Psi,L}}{M_{S_4}^2} x_4 \tilde{G}_Z(x_4, x_4) - \frac{2}{3} \frac{g^{\Psi,R}}{M_{S_4}^2} \tilde{F}_Z(x_4, x_4) + \frac{g^{\Phi_4}}{3M_\Psi^2} \tilde{H}_Z(x_4, x_4) \right] \right. \\ & \left. - |g_2^3|^2 \left[ \frac{g^{\Psi,R}}{M_{S_2}^2} x_2 \tilde{G}_Z(x_2, x_2) - \frac{2}{3} \frac{g^{\Psi,L}}{M_{S_2}^2} \tilde{F}_Z(x_2, x_2) + \frac{g^{\Phi_3}}{3M_\Psi^2} \tilde{H}_Z(x_2, x_2) \right] \right\}, \end{aligned} \quad (65)$$

$$\begin{aligned} \Delta g_L^{\nu_\tau\nu_\tau}(m_Z^2) = & \frac{3m_Z^2}{32\pi^2} \left\{ |g_2^3|^2 \left[ \frac{g^{\Psi,L}}{M_{S_4}^2} x_4 \tilde{G}_Z(x_4, x_4) - \frac{2}{3} \frac{g^{\Psi,R}}{M_{S_4}^2} \tilde{F}_Z(x_4, x_4) + \frac{(g^{\Phi_2})_{22}}{3M_\Psi^2} \tilde{H}_Z(x_4, x_4) \right] \right. \\ & \left. - |g_2^3|^2 \left[ \frac{g^{\Psi,R}}{M_{S_2}^2} x_2 \tilde{G}_Z(x_2, x_2) - \frac{2}{3} \frac{g^{\Psi,L}}{M_{S_2}^2} \tilde{F}_Z(x_2, x_2) + \frac{(g^{\Phi_2})_{11}}{3M_\Psi^2} \tilde{H}_Z(x_2, x_2) \right] \right\}, \end{aligned} \quad (66)$$

$$\Delta g_R^{\tau\tau}(m_Z^2) = \Delta g_R^{\nu_\tau\nu_\tau}(m_Z^2) = 0. \quad (67)$$

Here,  $M_{S_i}$  ( $i = 1, \dots, 4$ ) and  $M_\Psi$  denote the masses of the scalar fields  $S_i$  and the fermion  $\Psi$ , respectively, and we have defined the mass ratios  $x_i \equiv M_\Psi^2/M_{S_i}^2$ .

Analogously, within the fermion-rich model, we calculate the one-loop corrections to the  $Z \rightarrow \bar{s}b$ ,  $\tau^+\tau^-$ , and  $\nu_\tau\bar{\nu}_\tau$  decay channels. The resulting contributions to the effective form factors are given by

$$\Delta g_L^{sb}(m_Z^2) = \frac{m_Z^2}{32\pi^2} g_1^{2*} g_1^3 \left[ \frac{(g^{F_1,L})_{22}}{M_S^2} y_3 \tilde{G}_Z(y_3, y_3) - \frac{2}{3} \frac{(g^{F_1,R})_{22}}{M_S^2} \tilde{F}_Z(y_3, y_3) + \frac{g^S}{3M_{\Psi_3}^2} \tilde{H}_Z(y_3, y_3) \right], \quad (68)$$

$$\Delta g_R^{sb}(m_Z^2) = \frac{m_Z^2}{32\pi^2} g_1^{2*} g_1^3 \left[ \frac{(g^{F_1,R})_{11}}{M_S^2} y_1 \tilde{G}_Z(y_1, y_1) - \frac{2}{3} \frac{(g^{F_1,L})_{11}}{M_S^2} \tilde{F}_Z(y_1, y_1) + \frac{g^S}{3M_{\Psi_1}^2} \tilde{H}_Z(y_1, y_1) \right], \quad (69)$$

for the quark sector, and

$$\Delta g_L^{\tau\tau}(m_Z^2) = \frac{3m_Z^2}{32\pi^2} |g_2^3|^2 \left[ \frac{g^{F_3,L}}{M_S^2} y_2 \tilde{G}_Z(y_2, y_2) - \frac{2}{3} \frac{g^{F_3,R}}{M_S^2} \tilde{F}_Z(y_2, y_2) + \frac{g^S}{3M_{\Psi_2}^2} \tilde{H}_Z(y_2, y_2) \right], \quad (70)$$

$$\Delta g_L^{\nu\tau\nu\tau}(m_Z^2) = \frac{3m_Z^2}{32\pi^2} |g_2^3|^2 \left[ \frac{g^{F_2,L}}{M_S^2} y_2 \tilde{G}_Z(y_2, y_2) - \frac{2}{3} \frac{g^{F_2,R}}{M_S^2} \tilde{F}_Z(y_2, y_2) + \frac{g^S}{3M_{\Psi_2}^2} \tilde{H}_Z(y_2, y_2) \right], \quad (71)$$

$$\Delta g_R^{\tau\tau}(m_Z^2) = \Delta g_R^{\nu\tau\nu\tau}(m_Z^2) = 0, \quad (72)$$

for the lepton sector. Here,  $M_S$  and  $M_{\Psi_k}$  (with  $k = 1, 2, 3$ ) denote the masses of the scalar field  $S$  and the vector-like fermions  $\Psi_k$ , respectively. The mass ratios are defined as  $y_k = M_{\Psi_k}^2/M_S^2$ .

To constrain the new physics parameters, we utilize the precision measurements of  $Z$ -pole observables performed at LEP [82]. Following the analysis in Refs. [83, 84], we adopt the following model-independent bounds on the effective leptonic form factors<sup>2</sup>:

$$\Delta g_L^{\tau\tau}(m_Z^2) = (0.16 \pm 0.58) \times 10^{-3}, \quad (73)$$

$$\Delta g_L^{\nu\nu}(m_Z^2) = -(0.40 \pm 0.21) \times 10^{-2}. \quad (74)$$

Regarding the  $Z \rightarrow \bar{s}b$  decay, we apply the upper limit  $\mathcal{B}(Z \rightarrow q\bar{q}') < 2.9 \times 10^{-3}$  at 95% C.L., which is derived from the consistency between the measured hadronic  $Z$  width and the SM prediction [85, 86]. As the SM contribution to this mode is negligible compared to the current experimental sensitivity [86], we assume the decay is dominated by the NP contribution. This yields the constraint:

$$\frac{m_Z}{12\pi\Gamma_Z} \frac{g_2^2}{c_W^2} (|\Delta g_L^{sb}|^2 + |\Delta g_R^{sb}|^2) < 2.9 \times 10^{-3}, \quad (75)$$

where  $\Gamma_Z$  is the total decay width of the  $Z$  boson. These constraints are subsequently used to delimit the viable parameter space for the couplings in both benchmark models.

## V. PHENOMENOLOGICAL ANALYSIS

Having established the analytical bounds from individual decay channels, in this section, we perform a combined analysis to delineate the viable parameter space. We begin by defining benchmark masses for the new particles consistent with LHC direct searches. Subsequently, we map the allowed regions for the Yukawa couplings under specific degeneracy schemes. Finally, we evaluate the maximum attainable branching ratios for  $B \rightarrow K^{(*)}\nu\bar{\nu}$  permitted by the global data.

Let us first establish specific benchmark values for the masses of the new scalars and fermions. For the fermion-rich model, following the analysis in Ref. [84] to ensure safety from current bounds [88, 89], we set the masses of the colored fermions to  $M_{\Psi_1} = M_{\Psi_3} = 3.15$  TeV, while assigning a moderate mass of 450 GeV to the scalar  $S$  and the fermion  $\Psi_2$  ( $M_S = M_{\Psi_2} = 450$  GeV). This specific mass spectrum places the model well beyond the reach of direct searches at the LHC [90].

For the scalar-rich model, we align the mass spectrum of the color-singlet sector with the previous case, setting  $M_{\Psi} = M_{S_2} = M_{S_4} = 450$  GeV. This choice is justified because these fields are colorless and share similar quantum numbers with their counterparts in the fermion-rich model ( $S$  and  $\Psi_2$ ), implying comparable phenomenological constraints. The masses of the colored scalars  $S_{1,3}$  are then constrained by their decay into the  $\Psi$  fermion. Analyses of 36  $\text{fb}^{-1}$  data at  $\sqrt{s} = 13$  TeV [91, 92] indicate that for the  $\Psi$  mass of 450 GeV, the lower bound on the colored scalar mass is approximately 1.10 TeV.

Accordingly, we define the following two benchmark points (BPs):

- **BP-I (Scalar-rich):**  $M_{\Psi} = M_{S_2} = M_{S_4} = 450$  GeV,  $M_{S_1} = M_{S_3} = 1.10$  TeV.
- **BP-II (Fermion-rich):**  $M_S = M_{\Psi_2} = 450$  GeV,  $M_{\Psi_1} = M_{\Psi_3} = 3.15$  TeV.

With the mass spectra established, we proceed to constrain the coupling constants. We require all dimensionless couplings to satisfy the perturbative unitarity condition,  $|g| \leq 1$ , and assume they are real for simplicity. While the fermion-rich model is described by five couplings ( $\{g_1^3, g_1^2, g_1^3, g_1^2, g_2^3\}$ ), the scalar-rich model nominally introduces a sixth,  $\{g_1^3, g_1^2, g_1^3, g_1^2, g_2^3, g_2^3\}$ .

<sup>2</sup> We note that our sign convention for the  $Z$  couplings aligns with Ref. [83] but is opposite to that of Ref. [84].

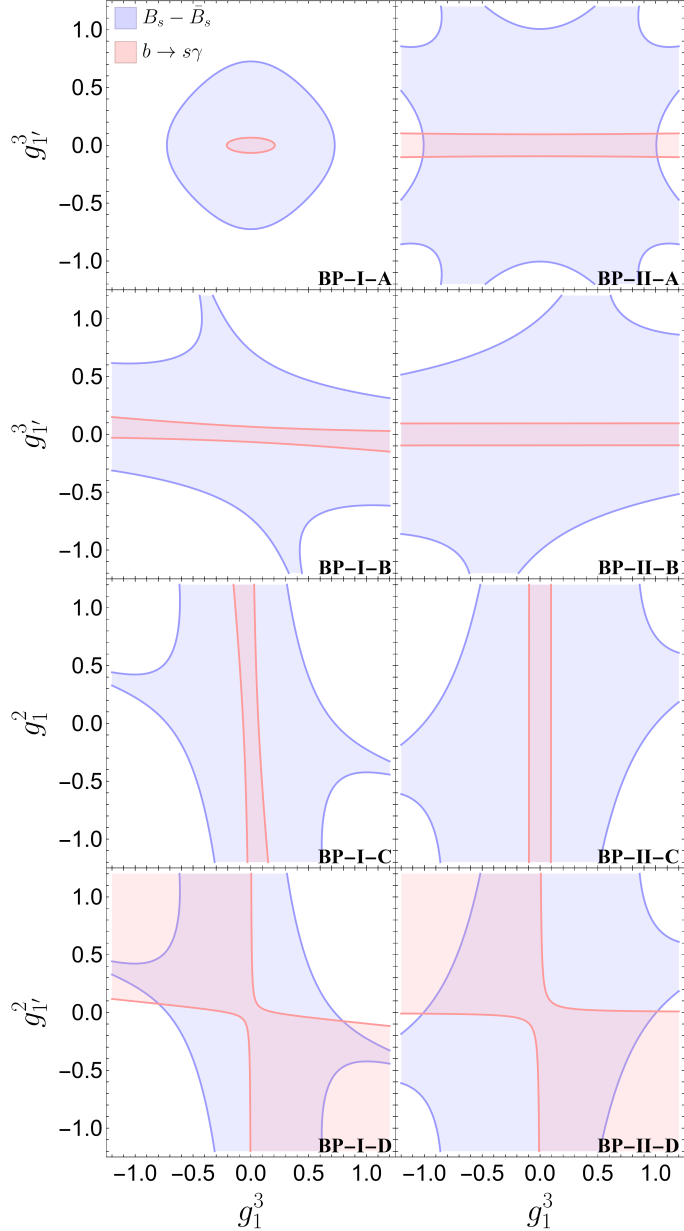


Figure 9. Allowed regions for the quark couplings in the scalar-rich (BP-I) and fermion-rich (BP-II) models under the four degeneracy schemes A–D. The blue and red shaded areas correspond to the parameter space consistent with  $B_s - \bar{B}_s$  mixing and  $b \rightarrow s\gamma$  constraints, respectively. The specific model and scheme are indicated in the bottom-right corner of each panel.

To simplify the analysis, we reduce the scalar-rich parameter space by assuming  $g_2^3 = g_{2'}^3$ , resulting in five independent constants for both models.

We note that the constraints derived from  $B_s - \bar{B}_s$  mixing,  $b \rightarrow s\gamma$ , and  $Z \rightarrow b\bar{s}$  act exclusively on the quark-sector couplings  $(g_1^3, g_1^2, g_{1'}^3, g_{1'}^2)$ . Similarly, the leptonic  $Z$ -pole observables ( $Z \rightarrow \tau^+\tau^-$  and  $Z \rightarrow \nu_\tau\bar{\nu}_\tau$ ) depend solely on the lepton coupling  $g_2^3$  (and  $g_{2'}^3$ ). We therefore utilize these processes to independently constrain the respective quark and lepton couplings. Our numerical evaluation reveals that the quark-sector couplings are strictly bounded by  $B_s - \bar{B}_s$  mixing and  $b \rightarrow s\gamma$ . Conversely, for the lepton coupling, we find that the constraints imposed by the leptonic  $Z$ -pole observables are less severe than the perturbative unitarity requirement.

In contrast, the semileptonic decays ( $B \rightarrow K^{(*)}\nu\bar{\nu}$  and  $b \rightarrow s\tau^+\tau^-$ ) involve the full set of couplings, making a direct analytical inversion to constrain the parameters infeasible. We therefore treat the experimental limits on these processes as additional conditions when determining the global maximum of the branching ratios  $\mathcal{B}(B^+ \rightarrow K^+\nu\bar{\nu})$  and  $\mathcal{B}(B^0 \rightarrow K^{*0}\nu\bar{\nu})$ .

Table IV. Maximum attainable branching ratios for  $B^+ \rightarrow K^+ \nu \bar{\nu}$  and  $B^0 \rightarrow K^{*0} \nu \bar{\nu}$  in the scalar-rich (BP-I) and fermion-rich (BP-II) models. The optimization is performed independently for the charged (left block) and neutral (right block) decay modes under the four coupling degeneracy schemes. The column “Param. Values” lists the specific configuration  $[x, y, z]$  that yields the maximum, where  $x \equiv (g_2^3)^2$ ,  $y \equiv g_1^3$ , and  $z$  represents the remaining independent parameter defined by the scheme. In cases where the maximum corresponds to the Standard Model limit, variables appearing as  $x, y$ , or  $z$  in the tuple indicate that the branching ratio is independent of that specific parameter (e.g.,  $(x, 0, 0)$  implies independence from  $x$  due to vanishing quark couplings). The predicted branching ratio for the complementary decay mode at this specific point is provided in the final column of each section.

Model	Scheme	$B^+ \rightarrow K^+ \nu \bar{\nu}$ Optimization			$B^0 \rightarrow K^{*0} \nu \bar{\nu}$ Optimization		
		$\mathcal{B}_{\max}$	Param. Values $[x, y, z]$	$\mathcal{B}(B^0 \rightarrow K^{*0} \nu \bar{\nu})$	$\mathcal{B}_{\max}$	Param. Values $[x, y, z]$	$\mathcal{B}(B^+ \rightarrow K^+ \nu \bar{\nu})$
BP-I	A	$4.16 \times 10^{-6}$	$(1, \pm 0.21, 0)$	$9.81 \times 10^{-6}$	$9.83 \times 10^{-6}$	$(x, 0, 0)$	$4.15 \times 10^{-6}$
	B	$4.16 \times 10^{-6}$	$(1, \pm 1, \pm 0.03)$	$9.81 \times 10^{-6}$	$9.88 \times 10^{-6}$	$(1, \pm 1, \mp 0.13)$	$4.10 \times 10^{-6}$
	C	$4.16 \times 10^{-6}$	$(1, \pm 0.03, \pm 1)$	$9.81 \times 10^{-6}$	$9.88 \times 10^{-6}$	$(1, \pm 0.13, \mp 1)$	$4.10 \times 10^{-6}$
	D	$4.60 \times 10^{-6}$	$(1, \pm 1, \mp 0.42)$	$9.68 \times 10^{-6}$	$1.01 \times 10^{-5}$	$(1, \pm 0.61, \mp 1)$	$4.45 \times 10^{-6}$
BP-II	A	$4.15 \times 10^{-6}$	$(0, y, z), (x, 0, 0)$	$9.83 \times 10^{-6}$	$1.00 \times 10^{-5}$	$(1, \pm 1, 0)$	$4.03 \times 10^{-6}$
	B	$4.16 \times 10^{-6}$	$(1, \pm 1, \mp 0.09)$	$9.81 \times 10^{-6}$	$9.84 \times 10^{-6}$	$(1, \pm 1, \pm 0.10)$	$4.13 \times 10^{-6}$
	C	$4.16 \times 10^{-6}$	$(1, \pm 0.09, \mp 1)$	$9.81 \times 10^{-6}$	$9.84 \times 10^{-6}$	$(1, \pm 0.10, \pm 1)$	$4.13 \times 10^{-6}$
	D	$4.17 \times 10^{-6}$	$(1, \pm 0.50, \mp 1)$	$1.00 \times 10^{-5}$	$1.00 \times 10^{-5}$	$(1, \pm 0.56, \mp 1)$	$4.17 \times 10^{-6}$

within the allowed parameter space set by the quark and lepton sector constraints.

To further simplify the phenomenological analysis of the remaining five free parameters  $(g_1^3, g_1^2, g_{1'}^3, g_{1'}^2, g_2^3)$ , we consider four distinct degeneracy schemes for the quark couplings:

- **Scheme A:**  $g_1^3 = g_1^2$ ,  $g_{1'}^3 = g_{1'}^2$ .

As illustrated in the BP-I-A panel of Fig. 9, the constraint from  $b \rightarrow s\gamma$  is generally more stringent than that from  $B_s - \bar{B}_s$  mixing. Under this scheme, the scalar-rich model (BP-I) is subject to significantly stronger constraints than the fermion-rich model (BP-II). Specifically, the viable parameter space for BP-I-A is restricted to a small, closed region, limiting  $g_1^3$  to the interval  $[-0.21, 0.21]$  and  $g_{1'}^3$  to  $[-0.07, 0.07]$ . In contrast, the  $b \rightarrow s\gamma$  constraint for BP-II-A manifests as a horizontal band extending across the entire perturbative range of  $g_1^3$ . Consequently, while  $g_1^3$  remains effectively unconstrained,  $g_{1'}^3$  is restricted to a narrow interval, which reaches its minimum width of  $[-0.10, 0.10]$  at  $g_1^3 = 0$ .

- **Scheme B:**  $g_1^2 = g_{1'}^3 = g_{1'}^2$ .

As depicted in the panels labeled BP-I-B and BP-II-B in Fig. 9,  $g_1^3$  remains largely unconstrained within the perturbative limit  $[-1, 1]$  for both models, while the common coupling is tightly bounded by  $b \rightarrow s\gamma$ . Specifically, the common coupling is restricted to approximately  $\pm 0.07$  for BP-I and  $\pm 0.10$  for BP-II.

- **Scheme C:**  $g_1^3 = g_{1'}^3 = g_1^2$ .

The resulting allowed regions (shown in panels BP-I-C and BP-II-C of Fig. 9) effectively mirror those of Scheme B with the axes interchanged, a consequence of the symmetric role these couplings play in the loop functions. Accordingly, the stringent constraints now apply to the group of couplings fixed to  $g_1^3$ , while  $g_1^2$  remains unconstrained over the range  $[-1, 1]$  in both models.

- **Scheme D:**  $g_1^3 = g_1^2 = g_{1'}^3$ .

As shown in the BP-I-D and BP-II-D panels of Fig. 9, the viable parameter space is notably larger compared to the previous schemes, indicating that decoupling  $g_{1'}^3$  from the other parameters provides considerable freedom to satisfy the flavor constraints. We observe that the allowed regions generally favor scenarios where  $g_1^3$  and  $g_{1'}^3$  exhibit opposite signs.

Having delineated the viable parameter space, we proceed to evaluate the maximum attainable branching ratios for  $B^+ \rightarrow K^+ \nu \bar{\nu}$  and  $B^0 \rightarrow K^{*0} \nu \bar{\nu}$ . For each benchmark point and degeneracy scheme, we perform independent numerical scans to maximize the decay rates of the charged and neutral modes. The results are summarized in Table IV. For each optimization case, we report the maximum branching fraction, the associated parameter values, and the corresponding prediction for the complementary decay channel.

In the case of BP-I-A, we find that NP contributions tend to suppress the neutral mode  $B^0 \rightarrow K^{*0} \nu \bar{\nu}$ . Consequently, its maximum branching ratio corresponds to the SM limit. This is represented by the parameter configuration  $(x, 0, 0)$ , where the vanishing quark couplings ( $y = z = 0$ ) render the specific value of the lepton coupling  $x$  irrelevant. Conversely, maximizing the  $B^+ \rightarrow K^+ \nu \bar{\nu}$  rate yields a modest 0.24% enhancement over the SM prediction; however, at this maximum, the predicted

rate for the neutral mode drops slightly below the SM value. This anti-correlation indicates that a simultaneous maximization of both decay modes is not possible under Scheme A. A similar pattern is observed for schemes BP-I-B and BP-I-C. Scheme D (BP-I-D), however, presents a distinct phenomenology: NP contributions provide constructive interference for both channels, allowing for maximal enhancements of 10.8% and 2.75% for the charged and neutral modes, respectively.

Turning to the fermion-rich model (BP-II), Scheme A exhibits the inverse behavior of the scalar-rich model. The NP contributions suppress the charged mode  $B^+ \rightarrow K^+ \nu \bar{\nu}$ , reducing its maximum to the SM value. This limit is reached via configurations such as  $(0, y, z)$  or  $(x, 0, 0)$ , where either the lepton or quark couplings vanish. Schemes B and C in BP-II follow the pattern seen in BP-I, where an enhancement in one channel typically comes at the cost of the other. In contrast, BP-II-D allows for a simultaneous maximization of both decay modes. Notably, the parameter configurations maximizing the charged and neutral rates are nearly identical, yielding enhancements of approximately 0.5% and 1.7% relative to the SM predictions, respectively.

Overall, our phenomenological analysis reveals that although the benchmark models can enhance the  $B \rightarrow K^{(*)} \nu \bar{\nu}$  branching ratios, the magnitude of these effects is insufficient to fully address the tension between the experimental measurements and the SM expectations. The NP contributions are severely constrained by the combined effect of the loop suppression factor inherent to the radiative generation mechanism and the tight experimental bounds on the couplings from  $B_s - \bar{B}_s$  mixing and  $b \rightarrow s\gamma$ . We therefore conclude that resolving the anomaly within these minimal one-loop frameworks is less favorable, unless the current tension is alleviated by future experimental updates or refined SM predictions.

## VI. CONCLUSION

In this work, we have addressed the emerging tension in flavor-changing neutral current transitions  $b \rightarrow s\nu\bar{\nu}$ , specifically the excess in the charged decay mode  $B^+ \rightarrow K^+ \nu \bar{\nu}$  observed by Belle II relative to the SM prediction and the limits on the neutral mode. These findings suggest the necessity of NP capable of generating both left-handed ( $\mathcal{O}_V^L$ ) and right-handed ( $\mathcal{O}_V^R$ ) effective operators.

Adopting a systematic bottom-up approach, we classified the renormalizable one-loop topologies capable of generating these operators. We identified the irreducible box diagram as the unique candidate for generating the relevant operators at the one-loop level without inducing tree-level contributions, provided that appropriate symmetries are imposed. Guided by gauge symmetry conservation, we cataloged the allowed quantum numbers for the internal mediators. From this classification, we proposed two minimal benchmark models for detailed study: a *scalar-rich model*, constructed by combining diagrams that independently generate  $\mathcal{O}_V^R$  and  $\mathcal{O}_V^L$ , and a *fermion-rich model*, where a single diagram topology is versatile enough to generate both operator chiralities.

We subjected these models to a comprehensive phenomenological analysis, constraining the parameter space using a complementary set of flavor observables and precision electroweak data. Under the assumption that the NP couples exclusively to the third lepton generation, our numerical evaluation reveals that the parameter space for both benchmark models is severely constrained, primarily by  $B_s - \bar{B}_s$  mixing and  $b \rightarrow s\gamma$ . In the analysis of degeneracy schemes where the quark couplings are correlated (Schemes A, B, and C), we observed an anti-correlation between the charged and neutral  $B \rightarrow K^{(*)} \nu \bar{\nu}$  modes; maximizing the branching ratio for one often leads to a suppression in the other. In the scenario where couplings are allowed to vary more freely (Scheme D), constructive interference permits simultaneous enhancements in both decay modes. However, due to the inherent loop suppression of the mechanism and the tight external constraints, the maximal attainable enhancements remain modest.

Ultimately, while the minimal one-loop models classified here can qualitatively address the need for right-handed currents, they struggle to quantitatively account for the large central value of the currently observed excess. Resolving the anomaly completely within these frameworks is less favorable unless future experimental measurements reduce the magnitude of the discrepancy or theoretical improvements refine the SM predictions.

## ACKNOWLEDGMENTS

This work is supported by the National Natural Science Foundation of China under Grants No. 12135006 and No. 12275067, the Natural Science Foundation of Henan Province under Grant No. 242300421390, the Science and Technology R&D Program Joint Fund Project of Henan Province under Grant No. 225200810030, the Science and Technology Innovation Leading Talent Support Program of Henan Province under Grant No. 254000510039, as well as the National Key R&D Program of China under Grant No. 2023YFA1606000.

## Appendix A: Loop-Integral Functions

This appendix provides the explicit analytical expressions for the loop-integral functions referenced in the main text. The evaluation of the NP contributions in the benchmark models (Sec. III) utilizes the following four-point integrals:

$$\begin{aligned} I_4(m_1, m_2, m_3, m_4) &\equiv \int \frac{d^d k}{(2\pi)^d i} \frac{1}{(k^2 - m_1^2)(k^2 - m_2^2)(k^2 - m_3^2)(k^2 - m_4^2)} \\ &= \frac{1}{(4\pi)^2} \left[ \frac{m_1^2}{(m_1^2 - m_2^2)(m_1^2 - m_3^2)(m_1^2 - m_4^2)} \ln \frac{m_4^2}{m_1^2} \right. \\ &\quad + \frac{m_2^2}{(m_2^2 - m_1^2)(m_2^2 - m_3^2)(m_2^2 - m_4^2)} \ln \frac{m_4^2}{m_2^2} \\ &\quad \left. + \frac{m_3^2}{(m_3^2 - m_1^2)(m_3^2 - m_2^2)(m_3^2 - m_4^2)} \ln \frac{m_4^2}{m_3^2} \right], \end{aligned} \quad (\text{A1})$$

$$\begin{aligned} J_4(m_1, m_2, m_3, m_4) &\equiv \int \frac{d^d k}{(2\pi)^d i} \frac{k^2}{(k^2 - m_1^2)(k^2 - m_2^2)(k^2 - m_3^2)(k^2 - m_4^2)} \\ &= \frac{1}{(4\pi)^2} \left[ \frac{m_1^4}{(m_1^2 - m_2^2)(m_1^2 - m_3^2)(m_1^2 - m_4^2)} \ln \frac{m_4^2}{m_1^2} \right. \\ &\quad + \frac{m_2^4}{(m_2^2 - m_1^2)(m_2^2 - m_3^2)(m_2^2 - m_4^2)} \ln \frac{m_4^2}{m_2^2} \\ &\quad \left. + \frac{m_3^4}{(m_3^2 - m_1^2)(m_3^2 - m_2^2)(m_3^2 - m_4^2)} \ln \frac{m_4^2}{m_3^2} \right]. \end{aligned} \quad (\text{A2})$$

Additionally, the analysis of the radiative decay  $b \rightarrow s\gamma$  in Sec. IV D involves the auxiliary loop functions  $F_7(x)$  and  $\tilde{F}_7(x)$ , which are defined as:

$$\begin{aligned} F_7(x) &= \frac{x^3 - 6x^2 + 3x + 6x \log x + 2}{12(x-1)^4}, \\ \tilde{F}_7(x) &= x^{-1} F_7(x^{-1}). \end{aligned} \quad (\text{A3})$$

## Appendix B: One-loop Corrections to $Z\bar{f}_i f_j$ Couplings

In this section, we revisit the radiative corrections to the couplings between the  $Z$  boson and two SM fermions,  $f_i$  and  $f_j$ , induced by the new physics sector. We consider general momentum transfer  $q^2$  to accommodate both on-shell  $Z$  decays and off-shell exchange processes. The effective Lagrangian governing the  $Z\bar{f}_i f_j$  interaction is defined as

$$\mathcal{L}_{\text{eff}} = \frac{g_2}{c_W} \bar{f}_i \gamma^\mu \left[ g_L^{ij}(q^2) P_L + g_R^{ij}(q^2) P_R \right] f_j Z_\mu + \text{h.c.}, \quad (\text{B1})$$

where  $q$  is the four-momentum of the  $Z$  boson,  $g_2$  is the  $SU(2)_L$  gauge coupling, and  $c_W \equiv \cos \theta_W$ , with  $\theta_W$  being the weak mixing angle. The form factors are decomposed into the tree-level SM contribution and the new physics loop correction:

$$g_{L(R)}^{ij}(q^2) = g_{L(R)}^{\text{SM}} \delta_{ij} + \Delta g_{L(R)}^{ij}(q^2). \quad (\text{B2})$$

The tree-level SM couplings are given by

$$g_L^{\text{SM}} = T_{f_i}^3 - Q_{f_i} s_W^2, \quad g_R^{\text{SM}} = -Q_{f_i} s_W^2, \quad (\text{B3})$$

where  $T_f^3$  is the third component of weak isospin and  $Q_f$  is the electric charge.

The relevant Feynman diagrams contributing to these corrections are depicted in Fig. 8. The interactions of the  $Z$  boson with the new scalars and fermions below the electroweak scale are parameterized by the following Lagrangian:

$$\mathcal{L}_Z = \frac{g_2}{c_W} Z_\mu \left( \bar{\Psi}_A \gamma^\mu \left[ g_{A,B}^{\Psi,L} P_L + g_{A,B}^{\Psi,R} P_R \right] \Psi_B + g_{MN}^\Phi \Phi_M^\dagger i \overleftrightarrow{\partial}^\mu \Phi_N \right) + \text{h.c.}, \quad (\text{B4})$$

where we utilize the notation  $a\overleftrightarrow{\partial}^{\mu}b \equiv a(\partial^{\mu}b) - (\partial^{\mu}a)b$ . The indices  $A, B$  (for fermions  $\Psi$ ) and  $M, N$  (for scalars  $\Phi$ ) implicitly run over all relevant internal degrees of freedom, including flavor, color, and  $SU(2)$  indices. The Yukawa interactions linking a new scalar  $\Phi_M$  and a new fermion  $\Psi_A$  to a SM fermion  $f_i$  are given by

$$\mathcal{L}_{\text{int}} = \bar{\Psi}_A \left( L_{AM}^{f_i} P_L + R_{AM}^{f_i} P_R \right) f_i \Phi_M + \text{h.c.} \quad (\text{B5})$$

We calculate the loop contributions to the form factors  $\Delta g_{L,R}^{ij}(q^2)$  using the Lagrangians in Eqs. (B4) and (B5). The calculation is performed with the aid of PACKAGE-X 2.1.1 [93, 94], adopting the covariant derivative convention and Feynman rules from Ref. [95]. In our evaluation, we adopt the limit of vanishing external SM fermion masses ( $m_{i,j} \rightarrow 0$ ) for both vertex and external leg corrections. An exception is made for the contributions proportional to  $\delta_{AB}\delta_{MN}$  involving the denominator ( $m_j^2 - m_i^2$ ), where setting the masses directly to zero would result in a kinematic singularity. We therefore retain the mass dependence in these specific terms to regulate the expression. We observe that in the limit where the tree-level couplings are flavor-diagonal ( $g_{f_i L}^{\text{SM}} = g_{f_j L}^{\text{SM}}$ )—as holds true in the SM—this singularity cancels out exactly, yielding a finite result consistent with the massless approximation.

The resulting left-handed contribution  $\Delta g_L^{ij}(q^2)$  is found to be:

$$\begin{aligned} \Delta g_L^{ij}(q^2) = & -\frac{\chi_Z L_{AM}^{i*} L_{BN}^j}{16\pi^2} \left\{ \left[ g_{f_j L}^{\text{SM}} \frac{m_i^2}{m_j^2 - m_i^2} B_1(m_i^2; M_{\Psi_A}, M_{\Phi_N}) \right. \right. \\ & - g_{f_i L}^{\text{SM}} \frac{m_j^2}{m_j^2 - m_i^2} B_1(m_j^2; M_{\Psi_A}, M_{\Phi_N}) \left. \right] \delta_{AB} \delta_{MN} \\ & + \left[ g_{AB}^L M_{\Psi_A} M_{\Psi_B} C_0(0, q^2, 0; M_{\Phi_N}, M_{\Psi_B}, M_{\Psi_A}) \right. \\ & - g_{AB}^R \left( B_0(q^2; M_{\Psi_B}, M_{\Psi_A}) + M_{\Phi_N}^2 C_0(0, q^2, 0; M_{\Phi_N}, M_{\Psi_B}, M_{\Psi_A}) \right. \\ & \left. \left. - 2C_{00}(0, q^2, 0; M_{\Phi_N}, M_{\Psi_B}, M_{\Psi_A}) \right) \right] \delta_{MN} \\ & \left. + 2g_{MN}^{\Phi} C_{00}(0, q^2, 0; M_{\Psi_A}, M_{\Phi_N}, M_{\Phi_M}) \delta_{AB} \right\}, \end{aligned} \quad (\text{B6})$$

and the right-handed contribution follows via the exchange of chirality parameters:

$$\Delta g_R^{ij}(q^2) = \Delta g_L^{ij}(q^2) (L \leftrightarrow R). \quad (\text{B7})$$

Here,  $B_{0,1}$ ,  $C_0$ , and  $C_{00}$  denote the Passarino-Veltman scalar integrals [93], and  $\chi_Z$  represents the relevant group theory factor (e.g., color factor).

For phenomenological applications where the new physics scale is significantly heavier than the momentum transfer, it is useful to expand the results in powers of  $q^2$ . Up to the first order in  $q^2$ , the form factors are

$$\begin{aligned} \Delta g_L^{ij}(q^2) = & \frac{\chi_Z L_{AM}^{i*} L_{BN}^j}{32\pi^2} \left\{ 2g_{AB}^L \delta_{MN} \frac{M_{\Psi_B} M_{\Psi_A}}{M_{\Phi_M}^2} G_Z(x_{AM}, x_{BM}) \right. \\ & - g_{AB}^R \delta_{MN} F_Z(x_{AM}, x_{BM}, M_{\Phi_M}) - g_{MN}^{\Phi} \delta_{AB} H_Z(x_{AM}, x_{BM}, M_{\Psi_A}) \\ & - g_{f_i L}^{\text{SM}} \delta_{AB} \delta_{MN} I_Z(x_{AM}, M_{\Phi_M}) \\ & + q^2 \left[ g_{AB}^L \delta_{MN} \frac{M_{\Psi_B} M_{\Psi_A}}{M_{\Phi_M}^4} \tilde{G}_Z(x_{AM}, x_{BM}) - \frac{2}{3} \frac{g_{AB}^R \delta_{MN}}{M_{\Phi_M}^2} \tilde{F}_Z(x_{AM}, x_{BM}) \right. \\ & \left. \left. + \frac{g_{MN}^{\Phi} \delta_{AB}}{3M_{\Psi_A}^2} \tilde{H}_Z(x_{AM}, x_{BM}) \right] \right\}, \end{aligned} \quad (\text{B8})$$

where we have defined the mass ratios  $x_{AM} \equiv M_{\Psi_A}^2/M_{\Phi_M}^2$ . The loop functions are defined as:

$$\begin{aligned}
G_Z(x, y) &= xF_V(x, y) + (x \leftrightarrow y), \\
F_Z(x, y, m) &= [x^2 F_V(x, y) + (x \leftrightarrow y)] - \frac{1}{2} - \overline{\text{div}}_\varepsilon, \\
H_Z(x, y, m) &= [yF_V(x, y) + (x \leftrightarrow y)] + \frac{3}{2} + \overline{\text{div}}_\varepsilon, \\
I_Z(x, m) &= \frac{3x - 1}{2(x - 1)} - x^2 F_V(x, 1) + \overline{\text{div}}_\varepsilon, \\
\tilde{G}_Z(x, y) &= xK_V(x, y) + (x \leftrightarrow y), \\
\tilde{F}_Z(x, y) &= \left[ x^2 K_V(x, y) - \frac{x^2}{x - y} F_V(x, y) \right] + (x \leftrightarrow y), \\
\tilde{H}_Z(x, y) &= \left[ \frac{x^2 y}{(y - 1)(x - y)^2} - \frac{x^2 y^2 (3x - y - 2) \log(x)}{(x - 1)^2 (x - y)^3} \right] + (x \leftrightarrow y), \tag{B9}
\end{aligned}$$

where the divergence parameter is given by  $\overline{\text{div}}_\varepsilon = \Delta_\varepsilon - \log(m^2/\mu^2)$  in dimensional regularization. The auxiliary functions  $F_V$  and  $K_V$  are

$$F_V(x, y) = \frac{\log(x)}{(x - 1)(x - y)}, \quad K_V(x, y) = \frac{(x^2 + xy - 2y) \log(x)}{(x - 1)^2 (x - y)^3} - \frac{1}{(x - 1)(x - y)^2}. \tag{B10}$$

We note that our analytical results differ slightly from those reported in Ref. [84]. Specifically, we observe an overall sign difference in the terms proportional to  $g_{MN}^\Phi$ , along with minor discrepancies in the finite parts of the loop functions  $F_Z$ ,  $H_Z$ , and  $I_Z$ . However, the physical behavior at  $q^2 = 0$  remains consistent. Since the NP sector introduces no new sources of electroweak symmetry breaking, the contributions from self-energies exactly cancel those from vertex corrections at zero momentum transfer. We confirm that our expressions for  $\Delta g_{L,R}^{ij}(q^2)$  vanish at  $q^2 = 0$ , in agreement with the limiting behavior established in Ref. [84].

### Appendix C: Quantum numbers of the internal fields and UV completions

In Sec. II, we derived physical model diagrams from the underlying topologies by imposing SM gauge invariance. While the allowed quantum numbers for diagram (c) (Fig. 3) were presented in Table I as a representative example, this appendix provides the complete classification for the remaining five topologies (Tables V–XI).

Connecting the high-scale UV models to the LEFT basis necessitates an intermediate matching onto the dimension-six SMEFT operators. Consequently, we calculate the Wilson coefficients for the relevant SMEFT operators generated by each diagram across all valid  $SU(2)_L$  assignments. The relative strengths of these contributions are summarized in Tables XII–XVIII.

Our calculation involves two distinct  $SU(2)_L$  contraction structures: vertices involving two doublets and an anti-triplet, and vertices involving a doublet, a triplet, and an anti-doublet (along with their Hermitian conjugates). To facilitate the evaluation of these contractions, we utilize two  $SU(2)_L$  tensors,  $\xi^A$  and  $\chi^A$ . The tensor  $\xi^A$ , defined in the main text, mediates interactions between two doublets and a triplet. For the second case, we introduce the tensor  $\chi^A$ , defined as:

$$\chi^A = \left( (\tau^1 + i\tau^2)/2, -\tau^3/\sqrt{2}, (-\tau^1 + i\tau^2)/2 \right), \quad A \in \{1, 2, 3\}, \tag{C1}$$

where  $\tau^i$  are the Pauli matrices:

$$\tau^1 = \begin{pmatrix} 0 & 1 \\ 1 & 0 \end{pmatrix}, \quad \tau^2 = \begin{pmatrix} 0 & -i \\ i & 0 \end{pmatrix}, \quad \tau^3 = \begin{pmatrix} 1 & 0 \\ 0 & -1 \end{pmatrix}.$$

The tensor  $\chi^A$  and its conjugate  $\chi^{A\dagger}$  govern the interaction vertices involving one doublet, one triplet, and one anti-doublet. In all cases, the index  $A$  corresponds to the  $SU(2)_L$  index of the triplet or anti-triplet field.

To illustrate the application of the  $\chi^A$  tensor, we consider Model A–VII based on diagram (c) (see Table I). Since the scalars  $X_2$  and  $X_4$  share identical SM quantum numbers in this model, we identify them as a single physical field ( $X_2 = X_4$ ). The explicit interaction Lagrangian, including the full  $SU(2)_L$  structure, is then given by:

$$\begin{aligned}
\mathcal{L} &\supset g_1^t \bar{\Psi}_1 Q_t X_2 + g_2^p \bar{L}_p \Psi_3 X_2^\dagger + g_2^{r*} \bar{\Psi}_3 L_r X_2 + g_1^{s*} \bar{Q}_s \Psi_1 X_2^\dagger \\
&= g_1^t \bar{\Psi}_{1\alpha} Q_{t\alpha'} X_2^A \chi_{\alpha\alpha'}^A + g_2^p \bar{L}_{p\beta} \Psi_{3\beta'} X_2^{*B} (\chi^{B\dagger})_{\beta\beta'} \\
&\quad + g_2^{r*} \bar{\Psi}_{3\rho} L_{r\rho'} X_2^{A'} \chi_{\rho\rho'}^{A'} + g_1^{s*} \bar{Q}_{s\sigma} \Psi_{1\sigma'} X_2^{*B'} (\chi^{B'\dagger})_{\sigma\sigma'}, \tag{C2}
\end{aligned}$$

where the Greek indices  $\alpha, \beta, \rho, \sigma$  run over the  $SU(2)_L$  doublet components 1, 2.

Table V. Possible assignments of quantum numbers under the  $SU(3)_c \otimes SU(2)_L \otimes U(1)_\alpha$  symmetry to the mediators in diagram (a) to generate the operator  $\mathcal{O}_V^R$ .

$SU(3)_c$	$\Psi_1$	$X_2$	$\Psi_3$	$X_4$
A	1	$\bar{3}$	1	1
B	3	1	3	3
$SU(2)_L$	$\Psi_1$	$X_2$	$\Psi_3$	$X_4$
I	1	1	1	2
II	2	2	2	1
III	2	2	2	3
IV	3	3	3	2
Y	$\Psi_1$	$X_2$	$\Psi_3$	$X_4$
	$\alpha$	$\alpha + 1/3$	$\alpha$	$\alpha - 1/2$

Table VI. Possible assignments of quantum numbers under the  $SU(3)_c \otimes SU(2)_L \otimes U(1)_\alpha$  symmetry to the mediators in diagram (b) to generate operator  $\mathcal{O}_V^R$ .

$SU(3)_c$	$\Psi_1$	$X_2$	$\Psi_3$	$X_4$
A	1	$\bar{3}$	$\bar{3}$	1
B	3	1	1	3
$SU(2)_L$	$\Psi_1$	$X_2$	$\Psi_3$	$X_4$
I	1	1	2	2
II	2	2	1	1
III	2	2	3	3
IV	3	3	2	2
Y	$\Psi_1$	$X_2$	$\Psi_3$	$X_4$
	$\alpha$	$\alpha + 1/3$	$\alpha - 1/6$	$\alpha - 1/2$

Table VII. Possible assignments of quantum numbers under the  $SU(3)_c \otimes SU(2)_L \otimes U(1)_\alpha$  symmetry to the mediators in diagram (c) to generate operator  $\mathcal{O}_V^R$ .

$SU(3)_c$	$\Psi_1$	$X_2$	$\Psi_3$	$X_4$
A	1	$\bar{3}$	$\bar{3}$	$\bar{3}$
B	3	1	1	1
$SU(2)_L$	$\Psi_1$	$X_2$	$\Psi_3$	$X_4$
I	1	1	2	1
II	2	2	1	2
III	2	2	3	2
IV	3	3	2	3
Y	$\Psi_1$	$X_2$	$\Psi_3$	$X_4$
	$\alpha$	$\alpha + 1/3$	$\alpha - 1/6$	$\alpha + 1/3$

Table VIII. Possible assignments of quantum numbers under the  $SU(3)_c \otimes SU(2)_L \otimes U(1)_\alpha$  symmetry to the mediators in diagram (d) to generate operator  $\mathcal{O}_V^L$ .

$SU(3)_c$	$\Psi_1$	$X_2$	$\Psi_3$	$X_4$
A	1	$\bar{3}$	$\bar{3}$	$\bar{3}$
B	3	1	1	1
$SU(2)_L$	$\Psi_1$	$X_2$	$\Psi_3$	$X_4$
I	1	2	1	2
II	1	2	3	2
III	2	1	2	1
IV	2	1	2	3
V	3	2	1	2
VI	3	2	3	2
VII	2	3	2	1
VIII	2	3	2	3
Y	$\Psi_1$	$X_2$	$\Psi_3$	$X_4$
	$\alpha$	$\alpha - 1/6$	$\alpha + 1/3$	$\alpha - 1/6$

Table IX. Possible assignments of quantum numbers under the  $SU(3)_c \otimes SU(2)_L \otimes U(1)_\alpha$  symmetry to the mediators in diagram (d) to generate operator  $\mathcal{O}_V^R$ .

$SU(3)_c$	$\Psi_1$	$X_2$	$\Psi_3$	$X_4$
A	1	$\bar{3}$	$\bar{3}$	$\bar{3}$
B	3	1	1	1
$SU(2)_L$	$\Psi_1$	$X_2$	$\Psi_3$	$X_4$
I	1	1	2	1
II	2	2	1	2
III	2	2	3	2
IV	3	3	2	3
Y	$\Psi_1$	$X_2$	$\Psi_3$	$X_4$
	$\alpha$	$\alpha + 1/3$	$\alpha + 5/6$	$\alpha + 1/3$

---

[1] I. Adachi *et al.* (Belle-II), [Phys. Rev. D \*\*109\*\*, 112006 \(2024\)](#), arXiv:2311.14647 [hep-ex].  
[2] D. Bećirević, G. Piazza, and O. Sumensari, [Eur. Phys. J. C \*\*83\*\*, 252 \(2023\)](#), arXiv:2301.06990 [hep-ph].  
[3] J. Grygier *et al.* (Belle), [Phys. Rev. D \*\*96\*\*, 091101 \(2017\)](#), [Addendum: Phys. Rev. D 97, 099902 (2018)], arXiv:1702.03224 [hep-ex].  
[4] T. E. Browder, N. G. Deshpande, R. Mandal, and R. Sinha, [Phys. Rev. D \*\*104\*\*, 053007 \(2021\)](#), arXiv:2107.01080 [hep-ph].  
[5] X. G. He and G. Valencia, [Phys. Lett. B \*\*821\*\*, 136607 \(2021\)](#), arXiv:2108.05033 [hep-ph].  
[6] T. Felkl, S. L. Li, and M. A. Schmidt, [JHEP \*\*12\*\*, 118 \(2021\)](#), arXiv:2111.04327 [hep-ph].  
[7] T. Felkl, A. Giri, R. Mohanta, and M. A. Schmidt, [Eur. Phys. J. C \*\*83\*\*, 1135 \(2023\)](#), arXiv:2309.02940 [hep-ph].  
[8] M. Ovchynnikov, M. A. Schmidt, and T. Schwetz, [Eur. Phys. J. C \*\*83\*\*, 791 \(2023\)](#), arXiv:2306.09508 [hep-ph].  
[9] L. Gärtner, N. Hartmann, L. Heinrich, M. Horstmann, T. Kuhr, M. Reboud, S. Stefkova, and D. van Dyk, [Eur. Phys. J. C \*\*84\*\*, 693 \(2024\)](#), arXiv:2402.08417 [hep-ph].  
[10] S. Rosauro-Alcaraz and L. P. S. Leal, [Eur. Phys. J. C \*\*84\*\*, 795 \(2024\)](#), arXiv:2404.17440 [hep-ph].  
[11] A. J. Buras, J. Harz, and M. A. Mojahed, [JHEP \*\*10\*\*, 087 \(2024\)](#), arXiv:2405.06742 [hep-ph].  
[12] D. Bećirević, S. Fajfer, N. Košnik, and L. Pavičić, [Phys. Lett. B \*\*861\*\*, 139285 \(2025\)](#), arXiv:2410.23257 [hep-ph].  
[13] A. Datta, D. Marfatia, and L. Mukherjee, [Phys. Rev. D \*\*109\*\*, L031701 \(2024\)](#), arXiv:2310.15136 [hep-ph].  
[14] C. Bird, P. Jackson, R. V. Kowalewski, and M. Pospelov, [Phys. Rev. Lett. \*\*93\*\*, 201803 \(2004\)](#), arXiv:hep-ph/0401195.  
[15] W. Altmannshofer, A. J. Buras, D. M. Straub, and M. Wick, [JHEP \*\*04\*\*, 022 \(2009\)](#), arXiv:0902.0160 [hep-ph].

Table X. Possible assignments of quantum numbers under the  $SU(3)_c \otimes SU(2)_L \otimes U(1)_\alpha$  symmetry to the mediators in diagram (e) to generate operator  $\mathcal{O}_V^L$ .

$SU(3)_c$	$\Psi_1$	$X_2$	$\Psi_3$	$X_4$
A	1	$\bar{3}$	1	1
B	3	1	3	3
$SU(2)_L$	$\Psi_1$	$X_2$	$\Psi_3$	$X_4$
I	1	2	1	2
II	1	2	3	2
III	2	1	2	3
IV	3	2	1	2
V	3	2	3	2
VI	2	3	2	1
VII	2	3	2	3
Y	$\Psi_1$	$X_2$	$\Psi_3$	$X_4$
	$\alpha$	$\alpha - 1/6$	$\alpha$	$\alpha + 1/2$

Table XI. Possible assignments of quantum numbers under the  $SU(3)_c \otimes SU(2)_L \otimes U(1)_\alpha$  symmetry to the mediators in diagram (f) to generate operator  $\mathcal{O}_V^L$ .

$SU(3)_c$	$\Psi_1$	$X_2$	$\Psi_3$	$X_4$
A	1	$\bar{3}$	$\bar{3}$	1
B	3	1	1	3
$SU(2)_L$	$\Psi_1$	$X_2$	$\Psi_3$	$X_4$
I	1	2	1	2
II	1	2	3	2
III	2	1	2	3
IV	3	2	1	2
V	3	2	3	2
VI	2	3	2	1
VII	2	3	2	3
Y	$\Psi_1$	$X_2$	$\Psi_3$	$X_4$
	$\alpha$	$\alpha - 1/6$	$\alpha + 1/3$	$\alpha + 1/2$

Table XII. Relative strengths of the SMEFT operator  $Q_{\ell d}$  generated by diagram (a) for the different  $SU(2)_L$  models. An overall normalization factor, which includes the loop function and couplings, is not presented.

Model Operator	I	II	III	IV
$Q_{\ell d}$	-1	1	$-3/2$	$-3/2$

- [16] X.-G. He, X.-D. Ma, and G. Valencia, [JHEP 03, 037 \(2023\)](#), arXiv:2209.05223 [hep-ph].
- [17] X.-G. He, X.-D. Ma, and G. Valencia, [Phys. Rev. D 109, 075019 \(2024\)](#), arXiv:2309.12741 [hep-ph].
- [18] B.-F. Hou, X.-Q. Li, M. Shen, Y.-D. Yang, and X.-B. Yuan, [JHEP 06, 172 \(2024\)](#), arXiv:2402.19208 [hep-ph].
- [19] X.-G. He, X.-D. Ma, M. A. Schmidt, G. Valencia, and R. R. Volkas, [JHEP 07, 168 \(2024\)](#), arXiv:2403.12485 [hep-ph].
- [20] S.-Y. Ho, J. Kim, and P. Ko, [Phys. Rev. D 111, 055029 \(2025\)](#), arXiv:2401.10112 [hep-ph].
- [21] M. Abdughani and Y. Reyimuaji, [Phys. Rev. D 110, 055013 \(2024\)](#), arXiv:2309.03706 [hep-ph].
- [22] A. Berezhnoy and D. Melikhov, [EPL 145, 14001 \(2024\)](#), arXiv:2309.17191 [hep-ph].

Table XIII. Relative strengths of the SMEFT operator  $Q_{\ell d}$  generated by diagram (b) for the different  $SU(2)_L$  models. An overall normalization factor, which includes the loop function and couplings, is not presented.

Model Operator	I	II	III	IV
$Q_{\ell d}$	-1	-1	$-3/2$	$-3/2$

Table XIV. Relative strengths of the SMEFT operator  $Q_{\ell d}$  generated by diagram (c) for the different  $SU(2)_L$  models. An overall normalization factor, which includes the loop function and couplings, is not presented.

Model Operator	I	II	III	IV
$Q_{\ell d}$	1	1	$3/2$	$3/2$

Table XV. Relative strengths of the SMEFT operators  $Q_{\ell q}^{(1)}$  and  $Q_{\ell q}^{(3)}$  generated by diagram (d) for the different  $SU(2)_L$  models. An overall normalization factor, which includes the loop function and couplings, is not presented.

Model Operator	I	II	III	IV	V	VI	VII	VIII
$Q_{\ell q}^{(1)}$	$-1/2$	$-3/4$	1	0	$-3/4$	$-9/8$	0	$-3/4$
$Q_{\ell q}^{(3)}$	$1/2$	$-1/4$	0	$1/2$	$1/4$	$1/8$	$-1/2$	$1/2$

Table XVI. Relative strengths of the SMEFT operator  $Q_{\ell d}$  generated by diagram (d) for the different  $SU(2)_L$  models. An overall normalization factor, which includes the loop function and couplings, is not presented.

Model Operator	I	II	III	IV
$Q_{\ell d}$	1	-1	$-3/2$	$-3/2$

Table XVII. Relative strengths of the SMEFT operators  $Q_{\ell q}^{(1)}$  and  $Q_{\ell q}^{(3)}$  generated by diagram (e) for the different  $SU(2)_L$  models. An overall normalization factor, which includes the loop function and couplings, is not presented.

Model Operator	I	II	III	IV	V	VI	VII
$Q_{\ell q}^{(1)}$	1	0	$3/4$	0	$9/8$	$3/4$	$9/8$
$Q_{\ell q}^{(3)}$	0	$1/2$	$-1/4$	$1/2$	$1/8$	$-1/4$	$1/8$

Table XVIII. Relative strengths of the SMEFT operators  $Q_{\ell q}^{(1)}$  and  $Q_{\ell q}^{(3)}$  generated by diagram (f) for the different  $SU(2)_L$  models. An overall normalization factor, which includes the loop function and couplings, is not presented.

Model Operator	I	II	III	IV	V	VI	VII
$Q_{\ell q}^{(1)}$	$1/2$	$-3/4$	$3/4$	$-3/4$	$-3/8$	$-3/4$	$3/8$
$Q_{\ell q}^{(3)}$	$-1/2$	$-1/4$	$-1/4$	$-1/4$	$-5/8$	$1/4$	$-5/8$

[23] Z. G. Berezhiani, M. Y. Khlopov, and R. R. Khomeriki, Sov. J. Nucl. Phys. **52**, 344 (1990).

[24] Z. G. Berezhiani and M. Y. Khlopov, Sov. J. Nucl. Phys. **51**, 935 (1990).

[25] Z. G. Berezhiani and M. Y. Khlopov, Sov. J. Nucl. Phys. **51**, 739 (1990).

[26] T. Ferber, A. Filimonova, R. Schäfer, and S. Westhoff, *JHEP* **04**, 131 (2023), arXiv:2201.06580 [hep-ph].

[27] W. Altmannshofer, A. Crivellin, H. Haigh, G. Inguglia, and J. Martin Camalich, *Phys. Rev. D* **109**, 075008 (2024), arXiv:2311.14629 [hep-ph].

[28] W. Altmannshofer and S. Roy, (2024), arXiv:2411.06592 [hep-ph].

[29] G.-Q. Dai, C.-X. Yue, Y.-Y. Bu, and Y.-H. Wang, *Commun. Theor. Phys.* **76**, 095202 (2024).

[30] L. Calibbi, T. Li, L. Mukherjee, and M. A. Schmidt, *Phys. Rev. D* **112**, 075020 (2025), arXiv:2502.04900 [hep-ph].

[31] A. Filimonova, R. Schäfer, and S. Westhoff, *Phys. Rev. D* **101**, 095006 (2020), arXiv:1911.03490 [hep-ph].

[32] K. Fridell, M. Ghosh, T. Okui, and K. Tobioka, *Phys. Rev. D* **109**, 115006 (2024), arXiv:2312.12507 [hep-ph].

[33] Q.-Y. Hu, (2024), arXiv:2412.19084 [hep-ph].

[34] P. D. Bolton, S. Fajfer, J. F. Kamenik, and M. Novoa-Brunet, *Phys. Rev. D* **110**, 055001 (2024), arXiv:2403.13887 [hep-ph].

[35] E. Gabrielli, L. Marzola, K. Müürsepp, and M. Raidal, *Eur. Phys. J. C* **84**, 460 (2024), arXiv:2402.05901 [hep-ph].

[36] D. McKeen, J. N. Ng, and D. Tuckler, *Phys. Rev. D* **109**, 075006 (2024), arXiv:2312.00982 [hep-ph].

[37] H. Davoudiasl and M. Schnubel, *Phys. Rev. D* **110**, 075014 (2024), arXiv:2406.19455 [hep-ph].

[38] P. Athron, R. Martinez, and C. Sierra, *JHEP* **02**, 121 (2024), arXiv:2308.13426 [hep-ph].

[39] R. Bause, H. Gisbert, and G. Hiller, *Phys. Rev. D* **109**, 015006 (2024), arXiv:2309.00075 [hep-ph].

[40] L. Allwicher, D. Becirevic, G. Piazza, S. Rosauro-Alcaraz, and O. Sumensari, *Phys. Lett. B* **848**, 138411 (2024), arXiv:2309.02246 [hep-ph].

[41] C.-H. Chen and C.-W. Chiang, *Phys. Rev. D* **109**, 075004 (2024), arXiv:2309.12904 [hep-ph].

[42] F.-Z. Chen, Q. Wen, and F. Xu, *Eur. Phys. J. C* **84**, 1012 (2024), arXiv:2401.11552 [hep-ph].

[43] D. Marzocca, M. Nardecchia, A. Stanzione, and C. Toni, *Eur. Phys. J. C* **84**, 1217 (2024), arXiv:2404.06533 [hep-ph].

[44] S. Karmakar, A. Dighe, and R. S. Gupta, *Phys. Rev. D* **111**, 055002 (2025), arXiv:2404.10061 [hep-ph].

[45] C. Hati, J. Leite, N. Nath, and J. W. F. Valle, *Phys. Rev. D* **111**, 015038 (2025), arXiv:2408.00060 [hep-ph].

[46] L. Allwicher, M. Bordone, G. Isidori, G. Piazza, and A. Stanzione, *Phys. Lett. B* **861**, 139295 (2025), arXiv:2410.21444 [hep-ph].

[47] H.-J. Tian, H.-B. Fu, T. Zhong, Y.-X. Wang, and X.-G. Wu, *Phys. Rev. D* **111**, 076013 (2025), arXiv:2411.12141 [hep-ph].

[48] J. Alda, A. Mir, and S. Penaranda, (2024), arXiv:2412.15830 [hep-ph].

[49] P. S. B. Dev, S. Goswami, C. Majumdar, and D. Pachhar, *JHEP* **01**, 004 (2025), arXiv:2407.04670 [hep-ph].

[50] A. J. Buras and P. Stangl, (2024), arXiv:2412.14254 [hep-ph].

[51] B. Bhattacharya, A. Datta, G. Faisel, S. Khalil, and S. Roy, (2024), arXiv:2412.16115 [hep-ph].

[52] C.-H. Chen and C.-W. Chiang, *Phys. Rev. D* **110**, 075036 (2024), arXiv:2403.02897 [hep-ph].

[53] C. S. Kim, D. Sahoo, and K. N. Vishnudath, *Eur. Phys. J. C* **84**, 882 (2024), arXiv:2405.17341 [hep-ph].

[54] C.-Q. Zhang, J. Sun, Z.-P. Xing, and R.-L. Zhu, (2024), arXiv:2501.00512 [hep-ph].

[55] Z.-K. Liu, Y. Li, B.-F. Hou, and Q. Chang, (2025), arXiv:2512.21191 [hep-ph].

[56] E. Ma, *Phys. Rev. D* **73**, 077301 (2006), arXiv:hep-ph/0601225.

[57] J. Kubo, E. Ma, and D. Suematsu, *Phys. Lett. B* **642**, 18 (2006), arXiv:hep-ph/0604114.

[58] S.-P. Li, X.-Q. Li, X.-S. Yan, and Y.-D. Yang, *Eur. Phys. J. C* **82**, 1078 (2022), arXiv:2204.09201 [hep-ph].

[59] C.-Y. Yao and G.-J. Ding, *Phys. Rev. D* **97**, 095042 (2018), arXiv:1802.05231 [hep-ph].

[60] S. Centelles Chuliá, R. Cepedello, E. Peinado, and R. Srivastava, *JHEP* **10**, 093 (2019), arXiv:1907.08630 [hep-ph].

[61] E. E. Jenkins, A. V. Manohar, and P. Stoffer, *JHEP* **03**, 016 (2018), [Erratum: JHEP 12, 043 (2023)], arXiv:1709.04486 [hep-ph].

[62] Z. Bo *et al.* (PandaX), *Phys. Rev. Lett.* **134**, 011805 (2025).

[63] E. Aprile *et al.* (XENON), *Phys. Rev. Lett.* **131**, 041003 (2023).

[64] L. Lopez Honorez, E. Nezri, J. F. Oliver, and M. H. G. Tytgat, *JCAP* **02**, 028 (2007), arXiv:hep-ph/0612275.

[65] Y. Farzan, S. Pascoli, and M. A. Schmidt, *JHEP* **03**, 107 (2013), arXiv:1208.2732 [hep-ph].

[66] P. Arnan, L. Hofer, F. Mescia, and A. Crivellin, *JHEP* **04**, 043 (2017), arXiv:1608.07832 [hep-ph].

[67] A. J. Buras, J. Girkbach-Noe, C. Niehoff, and D. M. Straub, *JHEP* **02**, 184 (2015), arXiv:1409.4557 [hep-ph].

[68] J. Brod, M. Gorbahn, and E. Stamou, *PoS BEAUTY2020*, 056 (2021), arXiv:2105.02868 [hep-ph].

[69] T. Blake, G. Lanfranchi, and D. M. Straub, *Prog. Part. Nucl. Phys.* **92**, 50 (2017), arXiv:1606.00916 [hep-ph].

[70] R. Aaij *et al.* (LHCb), *Phys. Rev. Lett.* **118**, 251802 (2017), arXiv:1703.02508 [hep-ex].

[71] J. Albrecht, F. Bernlochner, M. Kenzie, S. Reichert, D. Straub, and A. Tully, (2017), arXiv:1709.10308 [hep-ph].

[72] M. Dong *et al.* (CEPC Study Group), (2018), arXiv:1811.10545 [hep-ex].

[73] C. Bobeth, T. Ewerth, F. Kruger, and J. Urban, *Phys. Rev. D* **64**, 074014 (2001), arXiv:hep-ph/0104284.

[74] J. P. Lees *et al.* (BaBar), *Phys. Rev. Lett.* **118**, 031802 (2017), arXiv:1605.09637 [hep-ex].

[75] A. J. Buras, M. Misiak, and J. Urban, *Nucl. Phys. B* **586**, 397 (2000), [Erratum: Nucl.Phys.B 1002, 116529 (2024)], arXiv:hep-ph/0005183.

[76] J. Aebrischer, C. Bobeth, A. J. Buras, and J. Kumar, *JHEP* **12**, 187 (2020), arXiv:2009.07276 [hep-ph].

[77] K. Heinicke (LHCb), in *55th Rencontres de Moriond on Electroweak Interactions and Unified Theories* (2021) arXiv:2105.08134 [hep-ex].

[78] E. Lunghi and J. Matias, *JHEP* **04**, 058 (2007), arXiv:hep-ph/0612166.

[79] T. Enomoto and R. Watanabe, *JHEP* **05**, 002 (2016), arXiv:1511.05066 [hep-ph].

[80] S. Banerjee *et al.* (Heavy Flavor Averaging Group (HFLAV)), (2024), arXiv:2411.18639 [hep-ex].

- [81] M. Misiak *et al.*, *Phys. Rev. Lett.* **114**, 221801 (2015), arXiv:1503.01789 [hep-ph].
- [82] S. Schael *et al.* (ALEPH, DELPHI, L3, OPAL, SLD, LEP Electroweak Working Group, SLD Electroweak Group, SLD Heavy Flavour Group), *Phys. Rept.* **427**, 257 (2006), arXiv:hep-ex/0509008.
- [83] A. Efrati, A. Falkowski, and Y. Soreq, *JHEP* **07**, 018 (2015), arXiv:1503.07872 [hep-ph].
- [84] P. Arnan, A. Crivellin, M. Fedele, and F. Mescia, *JHEP* **06**, 118 (2019), arXiv:1904.05890 [hep-ph].
- [85] G. Abbiendi *et al.* (OPAL), *Eur. Phys. J. C* **19**, 587 (2001), arXiv:hep-ex/0012018.
- [86] J. F. Kamenik, A. Korajac, M. Szewc, M. Tammaro, and J. Zupan, *Phys. Rev. D* **109**, L011301 (2024), arXiv:2306.17520 [hep-ph].
- [87] S. Navas *et al.* (Particle Data Group), *Phys. Rev. D* **110**, 030001 (2024).
- [88] M. Aaboud *et al.* (ATLAS), *JHEP* **11**, 195 (2017), arXiv:1708.09266 [hep-ex].
- [89] M. Aaboud *et al.* (ATLAS), *Phys. Rev. D* **97**, 112001 (2018), arXiv:1712.02332 [hep-ex].
- [90] A. Banerjee *et al.*, (2022), arXiv:2203.07270 [hep-ph].
- [91] D. Racco, A. Wulzer, and F. Zwirner, *JHEP* **05**, 009 (2015), arXiv:1502.04701 [hep-ph].
- [92] M. Aaboud *et al.* (ATLAS), *JHEP* **01**, 126 (2018), arXiv:1711.03301 [hep-ex].
- [93] H. H. Patel, *Comput. Phys. Commun.* **197**, 276 (2015), arXiv:1503.01469 [hep-ph].
- [94] H. H. Patel, *Comput. Phys. Commun.* **218**, 66 (2017), arXiv:1612.00009 [hep-ph].
- [95] A. Crivellin and L. Schnell, *Comput. Phys. Commun.* **271**, 108188 (2022), arXiv:2105.04844 [hep-ph].